Extremely correlated Fermi liquid of the t-J model in two dimensions

Peizhi Mai and B. Sriram Shastry
Physics Department, University of California, Santa Cruz, California 95064, USA

(Received 29 August 2018; published 5 November 2018)

We study the two-dimensional t-J model with second-neighbor hopping parameter t' and in a broad range of doping δ using a closed set of equations from the extremely correlated Fermi liquid theory. We obtain asymmetric energy distribution curves and symmetric momentum distribution curves of the spectral function, consistent with experimental data. We further explore the Fermi surface and local density of states for different parameter sets. Using the spectral function, we calculate the resistivity, Hall number, and spin susceptibility. The curvature change in the resistivity curves with varying δ is presented and connected to intensity loss in angle-resolved photoemission spectroscopy experiments. We also discuss the role of the superexchange J in the spectral function and the resistivity in the optimal to overdoped density regimes.

DOI: 10.1103/PhysRevB.98.205106

I. INTRODUCTION

The t-J model where extreme correlations are manifest plays a fundamentally important role in understanding the physics of correlated matter, including high-T_c superconductors [1,2]. Despite the large progress [3–10] made in numerically solving the t-J model and the related Hubbard model, very few analytical techniques are reliable to obtain the low-temperature physics in this model for a broad range of dopings due to its inherent difficulties including noncanonical algebra for Gutzwiller projected fermions and the lack of an obvious small parameter for perturbation expansion.

To tackle this challenge, we have recently developed the extremely correlated Fermi liquid (ECFL) theory [11,12]. It is a nonperturbative analytical theory employing Schwinger's functional differential equations of motion to deal with lattice fermions under extreme correlation $U \to \infty$. The ECFL theory uses a systematic expansion of a bounded parameter $\lambda \in [0, 1]$, analogous to the expansion parameter $\frac{1}{2S}$ in the Dyson-Maleev representation of spins [13] via canonical bosons, and therefore provides a controlled calculation for the t-J model. With recent advances in the theory [14], it is possible to represent the ECFL equations to any order in λ in terms of diagrams which are generalizations of the Feynman graphs, without having to consider previous orders.

The second-order $O(\lambda^2)$ ECFL theory gives a closed set of equations for the Green's function and has been described in detail in Ref. [15]. It has been benchmarked successfully [16,17] against the exact results from the single-impurity Anderson model and the dynamical mean field theory (DMFT) [3,18–20], in the case of the infinite-dimensional large-U Hubbard model. The benchmarking has also been carried out in the one-dimensional t-J model, where k-dependent behavior is inevitable, against the density matrix renormalization group (DMRG) technique. ECFL and DMRG compare well [21] in describing the spin-charge separation in a Tomonaga-Luttinger liquid and the relevant strongly k-dependent self-energy.

Recently in Ref. [15], we have applied the second-order ECFL theory to studying the 2D t-J model with a second-neighbor hopping parameter t'. We calculated the spectral function peak, quasiparticle weight, and resistivity from hole doping ($t' \leqslant 0$) to electron doping ($t' > 0$). The high thermal sensitivity in the spectral function and small quasiparticle weight indicate a suppression of an effective Fermi liquid temperature scale. The curvature of resistivity vs T changes between concave and convex upon a sign change in t', implying a change of the effective Fermi liquid temperature [17]. We also compute the optical conductivity and the nonresonant Raman susceptibilities in Ref. [22].

In the present work, we perform a more detailed study in the 2D t-J model. Apart from the spectral function peak height, we compute the energy distribution curves (EDCs) and momentum distribution curves (MDCs) which are measured in angle-resolved photoemission spectroscopy (ARPES) [23]. For the first time from a microscopic theory, we obtain an asymmetric EDC line shape and a rather symmetric MDC line shape, which are consistent with experimental observation [23]. The self-energy is also calculated. It is independent of k in the infinite-dimensional limit [16] and has strong k-dependence in 1D [21]. In 2D our calculation gives a weakly k-dependent self-energy in the normal (metallic) state. For this reason, we expect the vertex correction to be modest. Then we compute the resistivity within the bubble scheme neglecting the vertex corrections. Unlike Ref. [15], here we focus on the doping dependence of resistivity vs T curves at different t', corresponding to experimental observation [24]. Spin susceptibility and the NMR spin-lattice relaxation rate are also calculated with the ECFL Green's function and related to experiment [25,26]. At the end, we discuss the effect of the superexchange interaction and justify our choice of J.

This work is organized as follows: First we summarize the ECFL formalism to calculate the electron Green's function and introduce the parameter region in Sec. II. In Sec. III, we discuss the ECFL spectral properties, resistivity, Hall response, and spin susceptibility at a fixed typical superexchange J, as well as the effect of changing J. Section IV includes a conclusion and some remarks.

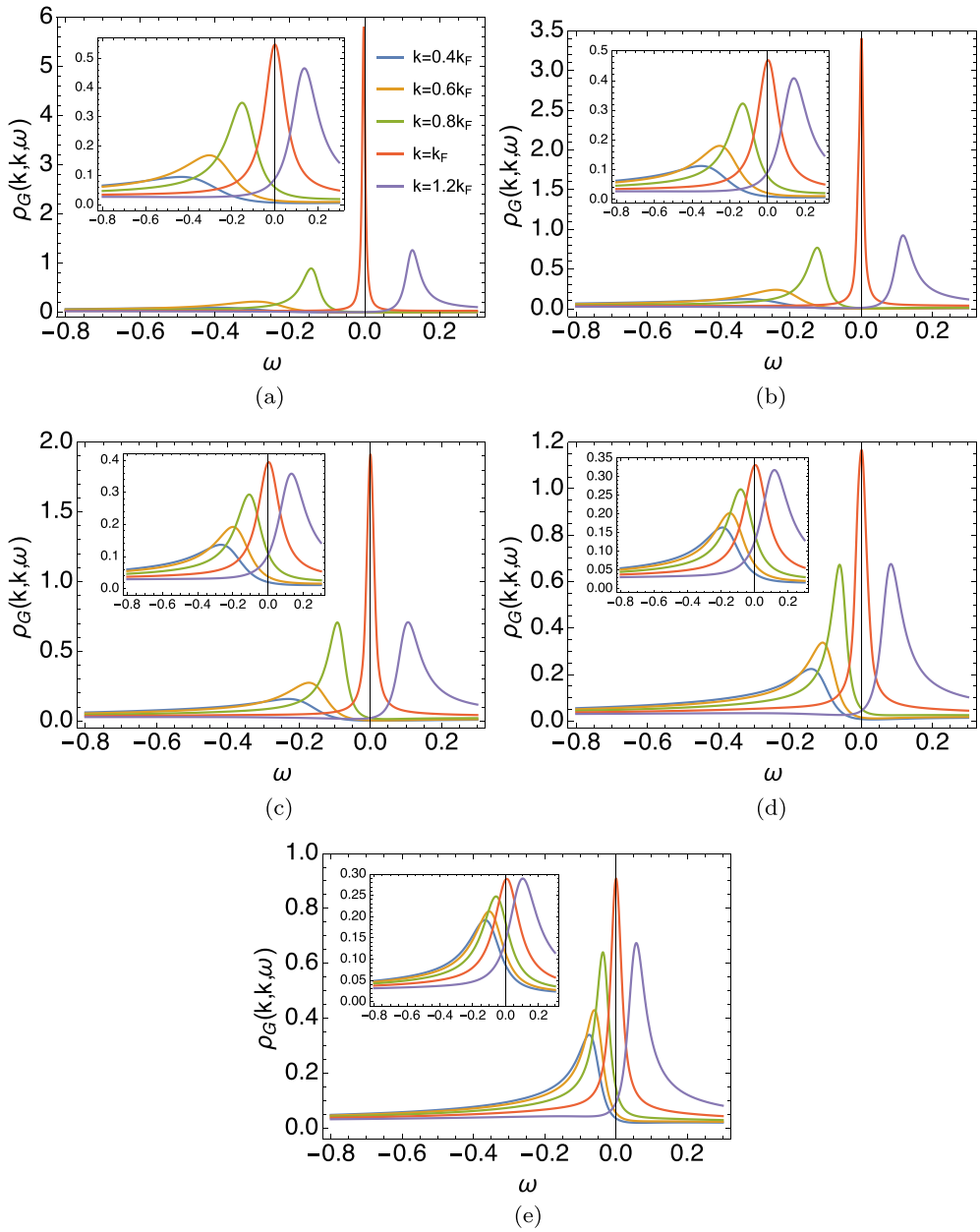

FIG. 1. EDC line shapes at different fixed values of momentum k in nodal direction ($\Gamma \to X$). All figures including insets share the same legend. The parameters are set as $\delta = 0.15$, $T = 105$ K or 400 K (inset) and t' as specified. The line peak and width in the vicinity of the Fermi surface depends strongly on temperature. The peak magnitude at $\omega = 0$ goes down as t' decreases due to stronger correlation. (a) $t' = 0.4$. (b) $t' = 0.2$. (c) $t' = 0$. (d) $t' = -0.2$. (e) $t' = -0.4$.

II. METHOD AND PARAMETERS

A. Summary of second-order ECFL theory

In the ECFL theory [11] the one-electron Green's function in momentum space is expressed as the product of an auxiliary Green's function $\mathbf{g}$ and a caparison function $\widetilde{\mu}$:

$$\mathcal{G}(k) = \mathbf{g}(k) \times \widetilde{\mu}(k), \tag{1}$$

where $k \equiv (\vec{k}, i\omega_n)$ and $\omega_n = (2n+1)\pi k_B T$ is the Matsubara frequency. Here $\mathbf{g}(k)$ is a canonical fermion propagator vanishing as $1/\omega$ as $\omega \to \infty$, and $\widetilde{\mu}(k)$ plays a role of adaptive spectral weight due to the noncanonical nature of the problem. In the minimal version of second-order theory [16] including superexchange J, they can be written explicitly as

$$\widetilde{\mu}(k) = 1 - \lambda\frac{n}{2} + \lambda\Psi(k), \tag{2}$$

$$\mathbf{g}^{-1}(k) = i\omega_n + \boldsymbol{\mu} - \frac{u_0}{2} + \frac{\lambda}{4}nJ_0 - \widetilde{\mu}(k)\varepsilon'_k - \lambda\chi(k), \tag{3}$$

where $\boldsymbol{\mu}$ is the chemical potential, and $\varepsilon'_k = \varepsilon_k - \frac{u_0}{2}$. Here u_0 is a Lagrange multiplier [27] guaranteeing the shift invariance of the t-J model at every order of λ. To elaborate, u_0 absorbs any arbitrary uniform shift of the band $\varepsilon_k \to \varepsilon_k + c$, a constant shift which should not change

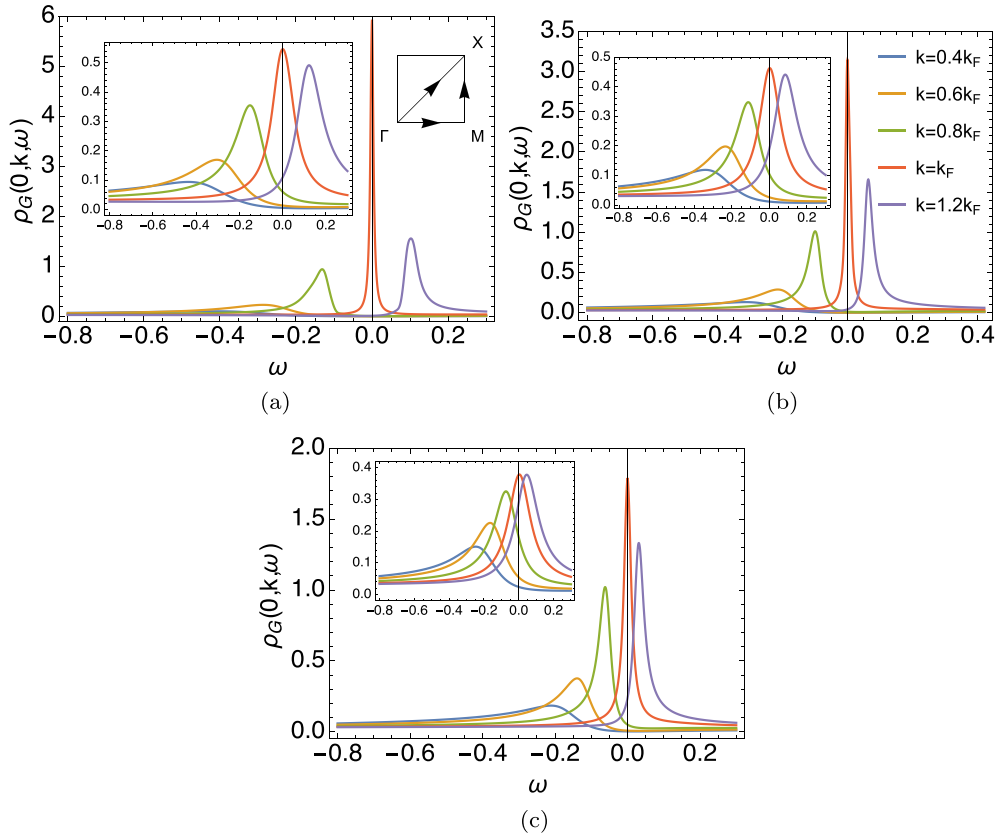

FIG. 2. EDC line shapes at different fixed values of momentum k in antinodal direction ($\Gamma \to M$). All figures including insets share the same legend. The parameters are set as $\delta = 0.15$, $T = 105$ K or 400 K (inset), and t' as specified. The line peak and width in the vicinity of the Fermi surface depend strongly on temperature. The peak magnitude at $\omega = 0$ goes down as t' decreases due to stronger correlation. (a) $t' = 0.4$. (b) $t' = 0.2$. (c) $t' = 0$.

the results. The band dispersion including next-nearest-neighbor hopping is $\varepsilon_k = -2t[\cos(k_x a_0) + \cos(k_y a_0)] - 4t' \cos(k_x a_0)\cos(k_y a_0)$, and Ψ and χ are two self-energy parts. These are given by [16]

$$\Psi(k) = -\sum_{pq} (\varepsilon'_p + \varepsilon'_q + J_{k-p}) \mathbf{g}(p)\mathbf{g}(q)\mathbf{g}(p+q-k), \quad (4)$$

$\chi = \chi_0 + \lambda\chi_1$ with $\chi_0 = -\sum_p \mathbf{g}(p)(\varepsilon'_p + \frac{1}{2}J_{k-p})$, and

$$\chi_1(k) = -\sum_{pq} \left[\varepsilon'_p + \varepsilon'_q + \frac{1}{2}(J_{k-p} + J_{k-q})\right] \times (\varepsilon'_{p+q-k} + J_{k-q})\mathbf{g}(p)\mathbf{g}(q)\mathbf{g}(p+q-k), \quad (5)$$

where $\sum_k \equiv \frac{k_B T}{N_s} \sum_{k_x,k_y,\omega_n}$, N_s is the number of sites, and $J_k = 2J(\cos k_x a_0 + \cos k_y a_0)$ is the nearest-neighbor exchange.

Denoting the particle and hole density per site by n and $\delta = 1 - n$, respectively, the two chemical potentials $\boldsymbol{\mu}$ and u_0 are determined through the number sum rules

$$\sum_k \mathbf{g}(k)\, e^{i\omega_n 0^+} = \frac{n}{2} = \sum_k \mathcal{G}(k)\, e^{i\omega_n 0^+}. \quad (6)$$

After analytically continuing $i\omega_n \to \omega + i0^+$ we determine the interacting electron spectral function $\rho_{\mathcal{G}}(\vec{k}, \omega) = -\frac{1}{\pi}\mathrm{Im}\mathcal{G}(\vec{k}, \omega)$. The set of equations (1)–(6) was solved iteratively on $L \times L$ lattices with $L = 61, 131, 181$ and a frequency grid with $N_\omega = 2^{14}$ points. $L > 61$ is usually for $t' \geqslant 0$ at low temperatures where the spectral function peak is higher and sharper than the negative t' cases; therefore it requires better k resolution.

B. Parameters in the programs

In this calculation, we set $t = 1$ as the energy scale and t' is varied between -0.4 and 0.4. We fix the superexchange to $J = 0.17$ unless otherwise specified because J usually is estimated to be in the region from 0 to 0.4, and has a small effect on the k-dependent behavior and barely influences the averaged physical quantities like resistivity, since the calculation includes a summation in k space. This argument will be further justified in the last part of Sec. III. Besides, we also explore a large region of doping δ from 0.11 to 0.3, where the second-order ECFL theory is reliable [16], and present the δ-dependent behavior at different t'. If not specified, ω is in units of t. According to Ref. [2], we assume $t = 0.45$ eV when using the absolute temperature scale.

C. The sign of t'

The significance of the sign of t' should be kept in mind, and the case $t' > 0$ is believed to correspond to electron-doped cuprate superconductors whereas $t' < 0$ is the hole-doped cuprates. The hole-doped case appears highly

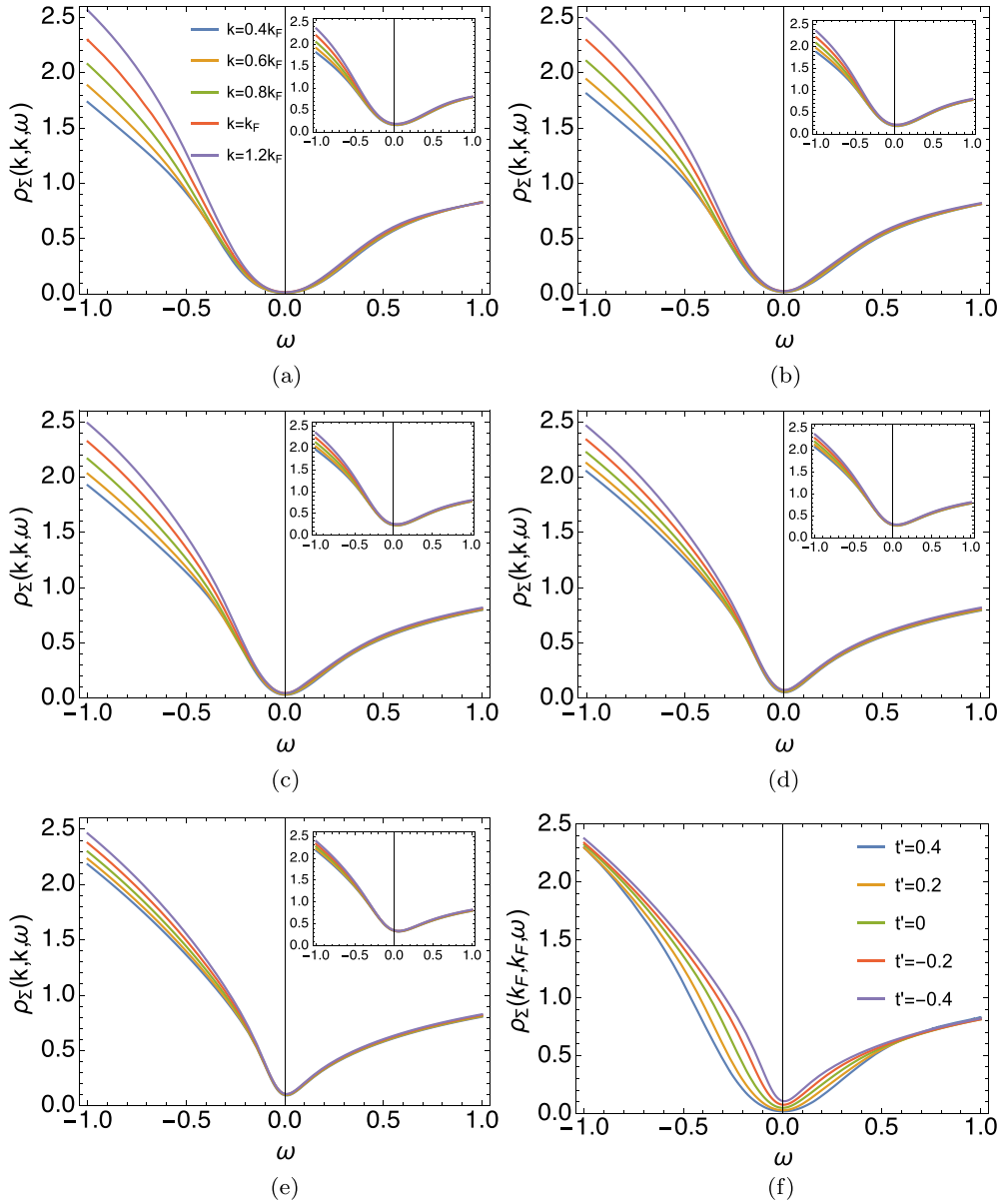

FIG. 3. (a)–(e) The negative imaginary part of self-energy ρ_Σ at different k in nodal ($\Gamma \to X$) direction with several t'. Here $\delta = 0.15$, $T = 105$ K and 400 K (inset). In all cases, ρ_Σ has a weak k dependence and differs mostly at high energy on the unoccupied side. Increasing temperature raises the bottom of the self-energy while leaving its high-energy part almost unchanged. (f) ρ_Σ at fixed $k = k_F$ in nodal direction varying t'. Increasing t' lowers the bottom of ρ_Σ and makes its low-energy part more rounded (Fermi-liquid-like). (a) $t' = 0.4$. (b) $t' = 0.2$. (c) $t' = 0$. (d) $t' = -0.2$. (e) $t' = -0.4$. (f) Varying t'.

non-Fermi-liquid-like as compared to the electron-doped case in experiments, and our earlier calculations as well as the present ones give a microscopic understanding of this important basic fact. We emphasize that despite this, the $t' > 0$ case is also strongly correlated, when we view the T dependence of the spectral features, where the effective Fermi scale is much reduced from the bare (band structure) value.

III. RESULTS

A. Spectral properties

1. Spectral function and self-energy

In earlier studies [23], the ECFL spectral function obtained phenomenologically [11,23,28] has been compared with experimental data measured with angle-resolved photoemission spectroscopy (ARPES) at optimal doping, leading to very good fits. Later we calculated the spectral function from the raw second-order ECFL equations in the symmetrized model [29] but it is only valid for doping $\delta \gtrsim 0.25$. Here we present the result at optimal doping $\delta = 0.15$ from a microscopic calculation of ECFL by numerically solving the improved set of second-order equations [15,16].

We display the energy distribution curves (EDCs) in Fig. 1 and Fig. 2, obtained by fixing k and scanning ω at optimal doping and various t'. These quantities can be measured in ARPES experiments. Figure 1 shows the EDCs for several constant k along the nodal ($\Gamma \to X$) and Fig. 2 for the antinodal direction ($\Gamma \to M$ for $t' > 0$). Note that the value of

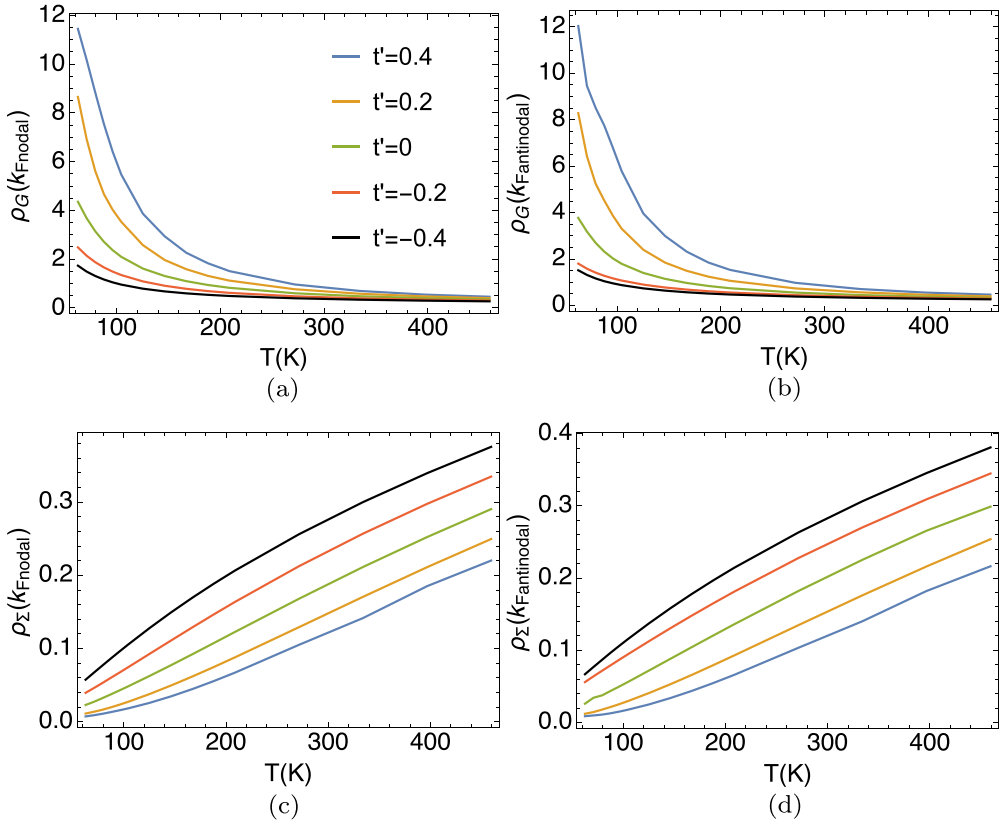

FIG. 4. The spectral functions at $\omega = 0$: ρ_G and ρ_Σ at k_F (in nodal and antinodal directions) vs T with varying t' at $\delta = 0.15$; legend is the same for each figure. (a) $\rho_G(k_{F\,\mathrm{nodal}})$. (b) $\rho_G(k_{F\,\mathrm{antinodal}})$. (c) $\rho_\Sigma(k_{F\,\mathrm{nodal}})$. (d) $\rho_\Sigma(k_{F\,\mathrm{antinodal}})$.

k_F depends on t' and direction in k space. The fixed value of k is given in terms of k_F based on the specific t' and direction. The antinodal $(M \to X)$ k_F for $t' \leqslant -0.2$ is close to zero. The corresponding EDCs are too close to resolve clearly; hence they are not presented.

We observe that at low temperatures the EDC peak gets sharper as k approaches the Fermi surface. The insets show that a small heating ($\Delta T \sim 0.06t$) strongly suppresses the region around the Fermi surface $k \sim k_F$ while it leaves the region away from Fermi surface almost unchanged. As a result, a weaker k dependence of peak height can be viewed in the higher temperature. It also shows that the EDC line shape is asymmetric for $k < k_F$, consistent with ARPES experiments. As t' decreases from positive (electron doped) to negative (hole doped), the correlation becomes stronger, and therefore the spectral peak gets lower. Slight anisotropy is found for $t' \leqslant 0.2$ in that the peak at the Fermi surface is a bit higher in the nodal direction than in the antinodal direction, indicating a weak k dependence of self-energy.

The spectral function of the Dyson self-energy is defined as

$$\rho_\Sigma(\vec{k}, \omega) = -\frac{1}{\pi}\mathrm{Im}\,\Sigma(\vec{k}, \omega). \tag{7}$$

It is calculated from the spectral function obtained from solving the set of ECFL equations (1)–(6):

$$\rho_\Sigma(\vec{k}, \omega) = \frac{\rho_G(\vec{k}, \omega)}{\pi^2\rho_G^2(\vec{k}, \omega) + [\mathrm{Re}G(\vec{k}, \omega)]^2}, \tag{8}$$

where ReG is calculated through Hilbert transform of ρ_G. As observed in Figs. 3(a)–3(e), the self-energy shows asymmetry from intermediate frequencies at essentially all values of t' and k, which is consistent with previous studies [16,29], unlike the symmetric curves in standard Fermi liquid theory. Further they all appear to depend weakly on k. This is qualitatively different from the strong k dependence of the low-energy behaviors of the self-energy in one dimension [21]. This weak k dependence supports our approximation of resistivity formula ignoring vertex correction in the next section. The inset indicates that the heating makes the most difference in the low-energy region by lifting the bottom. In Fig. 3(f), ρ_Σ at k_F for different t' are put together. As t' increase from negative to positive, its minimum goes down, indicating a lower decay rate, and the bottom region becomes rounded and more Fermi-liquid-like.

We also study the temperature-dependent $\rho_G(k_F)$ and $\rho_\Sigma(k_F)$ at $\omega = 0$ for k_F in the nodal and antinodal direction in Fig. 4. Also, panels (a) and (b) show that the spectral function peak is very sensitive to temperature changes. A sharp drop happens over a small temperature region (<1% bare bandwidth), wiping out the quasiparticle peak for $T > 400$ K in either direction. Another angle to observe this phenomenon is through the self-energy, $\rho_\Sigma(k_F) = 1/[\pi^2\rho_G(k_F)]$, describing the decay rate of a quasiparticle. The huge increase of $\rho_\Sigma(k_F)$ upon small warming shows a rapid drop in the lifetime of a quasiparticle. Note that the ρ_Σ curvature dependence on t' is similar to that of the plane resistivity in Fig. 4 of Ref. [15].

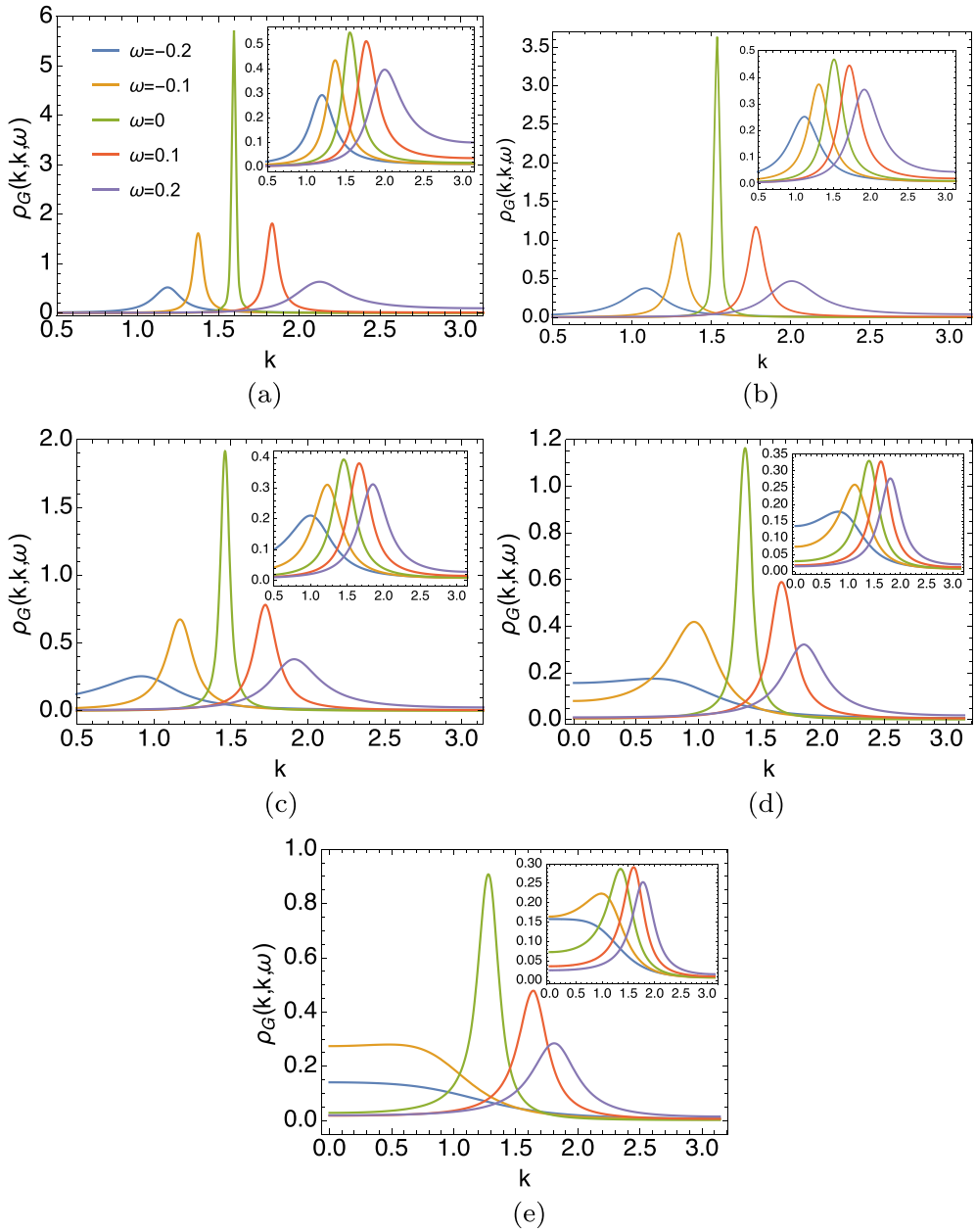

FIG. 5. MDC line shapes at different fixed values of frequency ω in each curve. All figures including insets share the legend. Here the parameters are set as $\delta = 0.15$, $T = 105$ K and 400 K (inset). k is scanned along the nodal ($\Gamma \to X$) direction. In all cases, they have a highest peak with a symmetric shape at $\omega = 0$. Consistently, the peak height decreases with smaller t', or stronger correlation. (a) $t' = 0.4$, nodal ($\Gamma \to X$). (b) $t' = 0.2$, nodal ($\Gamma \to X$). (c) $t' = 0$, nodal ($\Gamma \to X$). (d) $t' = -0.2$, nodal ($\Gamma \to X$). (e) $t' = -0.4$, nodal ($\Gamma \to X$).

The momentum distribution curves (MDCs) are plotted in Fig. 5 and Fig. 6, obtained by fixing ω and scanning k in nodal and antinodal directions, respectively, at optimal doping and various t'. As expected from the EDC case, the MDC peak is highest at the Fermi surface $\omega = 0$, which gets broadened the most upon warming. However, unlike the EDC case, the MDC peaks that are far away from $k = 0$ or π look more symmetric. This difference is consistent with experimental findings. The spectral function in the early phenomenological versions of ECFL, Refs. [23,28], leads to a somewhat exaggerated asymmetry in MDC curves, and has been the subject of further phenomenological adjustments in Ref. [30], to reconcile with experiments. The present microscopic results show that the greater symmetry of the MDC spectral lines comes about naturally, without the need for any adjustment of the parameters.

2. *Fermi surface*

The Fermi surface (FS) structure can be observed in the momentum distribution of spectral function peak height. We present the case for $t' = -0.2$, which is roughly the parameter describing the LSCO cuprate material [31], and vary the doping δ in Fig. 7. The FS is hole-like (open) for low doping [panels (a) and (b)] and becomes electron-like (closed) for high doping in panels (d) and (e). The transition

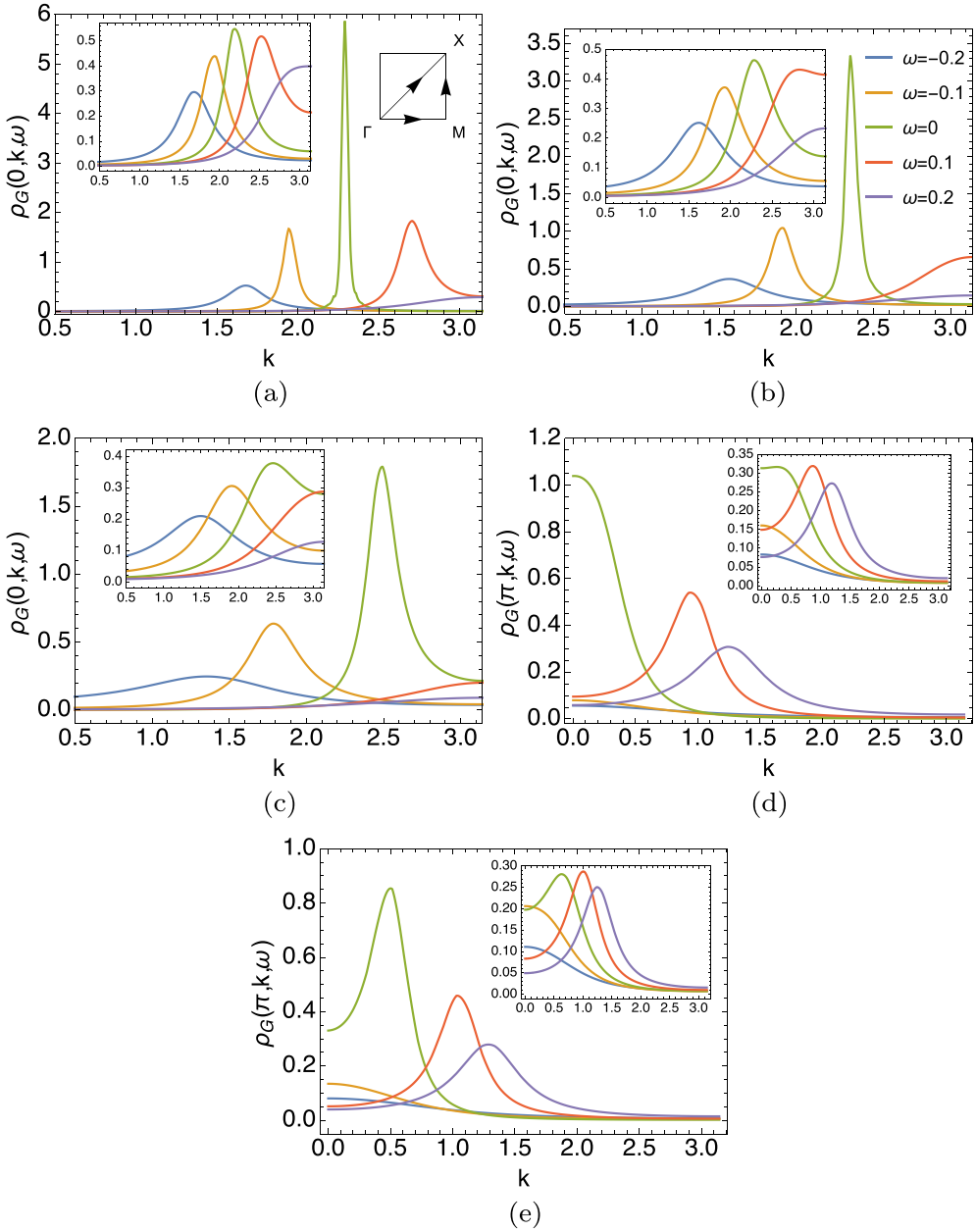

FIG. 6. MDC line shapes at different fixed values of frequency ω in each curve. All figures including insets share the same legend. Here the parameters are set as $\delta = 0.15$, $T = 105$ K and 400 K (inset). k is scanned along the antinodal ($\Gamma \to M$ for $t' \geqslant 0$ or $M \to X$ for $t' < 0$) directions. (a) $t' = 0.4$, antinodal ($\Gamma \to M$). (b) $t' = 0.2$, antinodal ($\Gamma \to M$). (c) $t' = 0$, antinodal ($\Gamma \to M$). (d) $t' = -0.2$, antinodal ($M \to X$). (e) $t' = -0.4$, antinodal ($M \to X$).

point $\delta \approx 0.17$ can be explicitly seen in Fig. 8(a) which is close to the noninteracting case with the tight-binding model in Fig. 8(e), consistent with experimental findings [31–33]. At higher (hole) doping which leads to a weaker effective correlation [15], the quasiparticle peak height increases and becomes more Fermi-liquid-like.

The FS is only well defined at zero temperature. Following Ref. [34] we can define a pseudo-FS at finite temperature, by examining a specifically weighted first moment of the energy:

$$\gamma_{k\sigma}(\mu, T) = -\int \rho_G(k, \omega) \times \frac{d\omega\, \omega}{\cosh(\beta\omega/2)} \Big/ \int \rho_G(k, \omega) \frac{d\omega}{\cosh(\beta\omega/2)}. \quad (9)$$

We *define* a pseudo-FS as the surface in $\vec{k}$ space where $\gamma_{k\sigma}$ changes sign from positive to negative. Shastry has recently shown [34] that at $T = 0$, the pseudo-FS becomes the exact Luttinger-Ward FS. It is further suggested that it is useful to study a T-dependent effective carrier density

$$N_{\text{eff}} = \sum_{k\sigma} \Theta(\gamma_{k\sigma}(\mu, T)), \quad (10)$$

where Θ is the Heaviside step function, such that $N_{\text{eff}} = N$ at zero temperature. At finite temperatures we expect that $N_{\text{eff}} \neq N$, and the difference between the two gives insights into the different T scales at play. This is especially applicable in strongly correlated materials, where it is well known [17–19]

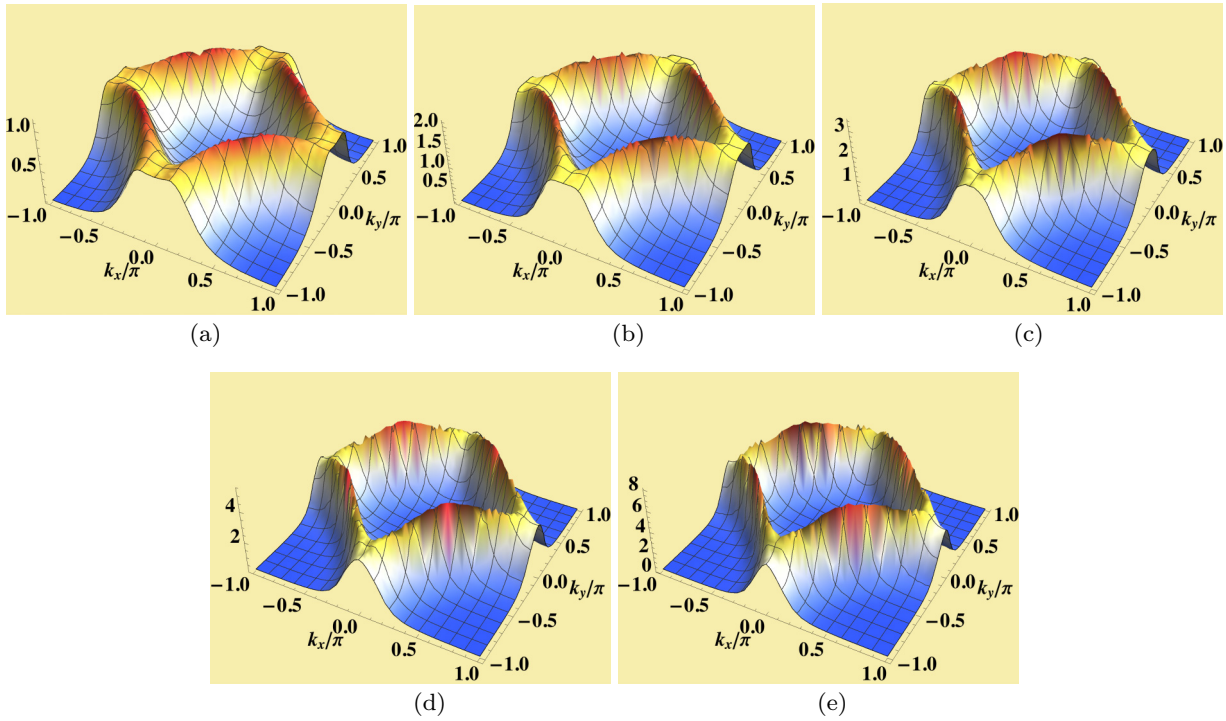

FIG. 7. The 3D plot of the spectral function peak height at several dopings at $t' = -0.2$, $T = 63$ K. The ridge in the spectral function peak tracks the Fermi surface. As δ increases, we find that the Fermi surface changes from open (hole-like) to close (electron-like), with the critical $\delta \approx 0.17$. The ridge height increases generally as δ goes up, showing decreasing correlation strength. (a) $\delta = 0.11$. (b) $\delta = 0.14$. (c) $\delta = 0.17$. (d) $\delta = 0.2$. (e) $\delta = 0.23$.

that Gutzwiller correlations result in the Fermi liquid regime, the strange-metal regime, and the bad-metal regime, followed by a high-T regime, with three crossover temperatures. In Fig. 9, we show how $N_{\rm eff}/N$ changes with temperature for different t'. For $t' \geqslant 0$, $N_{\rm eff}$ increases monotonically toward N as T goes down. And for $t' < 0$, $N_{\rm eff}$ decreases from larger to smaller than N upon cooling. With further lowering T one expects that $N_{\rm eff}$ equals N.

At low temperatures ($T \ll t$), we find that the roots of γ_k are close to the location of the ridge of spectral peak height shown in Fig. 11, and hence it can be taken as an approximate or a pseudo-finite-temperature FS. Figure 10 shows that the pseudo-FS is getting close to the true FS at zero temperature as T goes down for both electron-doped and hole-doped systems.

To understand better the deviations at finite T seen in Fig. 9, Fig. 10, and Fig. 11, it is helpful to recall a phenomenological spectral function [48] (see Eq. (9) and Eqs. (SI-20) and (SI-21) in Ref. [48]). This function is obtained by expanding the two self-energies in Eq. (2) and Eq. (3) at low energies in a power series. It captures many features of the ECFL calculations in terms of a few parameters, and is given as

$$A(\hat{k},\omega) = \frac{z_0}{\pi}\frac{\Gamma(\omega)}{\Gamma(\omega)^2 + (\omega - V_L\hat{k})^2}\left(1 - \frac{\xi}{\sqrt{1 + c_\alpha \xi^2}}\right), \quad (11)$$

where $\hat{k}$ is the component of $\vec{k}$ normal to the FS; $\xi = \frac{1}{\Delta_0}(\omega - r\ V_L\hat{k})$; $\Gamma(\omega) = \eta + \frac{\pi}{\Omega_\Phi}(\omega^2 + \pi^2 k_B^2 T^2)$; Δ_0 and Ω_Φ are the low- and high-energy scales; V_L is the Fermi velocity; and z_0, r, and c_α are numerical constants. The important variable $r \in [0, 2]$ determines the location of a feature in the dispersion known as the "kink." It is analyzed using this model spectral function in Ref. [48]. Here $r = 1$ is at the border of two regimes $r < 1$ with kinks in the unoccupied side, and $r > 1$ with kinks in the occupied side of the distribution. In Fig. 12 we plot the location of the peak in the spectral function Eq. (11) against T, for three values $r = 0.5$, 1, and 1.5. From this we see that these regimes display either a shrinking or an enlargement of the FS with increasing T. This corresponds to the types of behavior seen in Fig. 10 and Fig. 11.

3. *Local density of states*

The local density of states (LDOS) is calculated by $\sum_{\vec{k}}(1/N_s)\rho_G(\vec{k},\omega)$ and plotted in Figs. 13 and 14, varying t' with fixed $\delta = 0.15$ and varying δ with fixed $t' = 0, -0.4$, respectively. This quantity can be measured by scanning tunneling microscopy [35–39].

In Fig. 13, comparing panels (a) and (c), we observe that the LDOS peak gets smoothened and also broadened by the electron-electron interaction. Although the relative position for different t' remains unchanged after turning on interaction, the strong correlation brings them closer by renormalizing the bare band into the effective one, as shown in the inset of Fig. 22. From panel (a) to (b), raising temperature tends to have a stronger suppression on the peak with lower t'. This means the system with higher t' has a higher Fermi liquid temperature scale, and therefore it is more robust to heating, which is consistent with the previous findings of the spectral function.

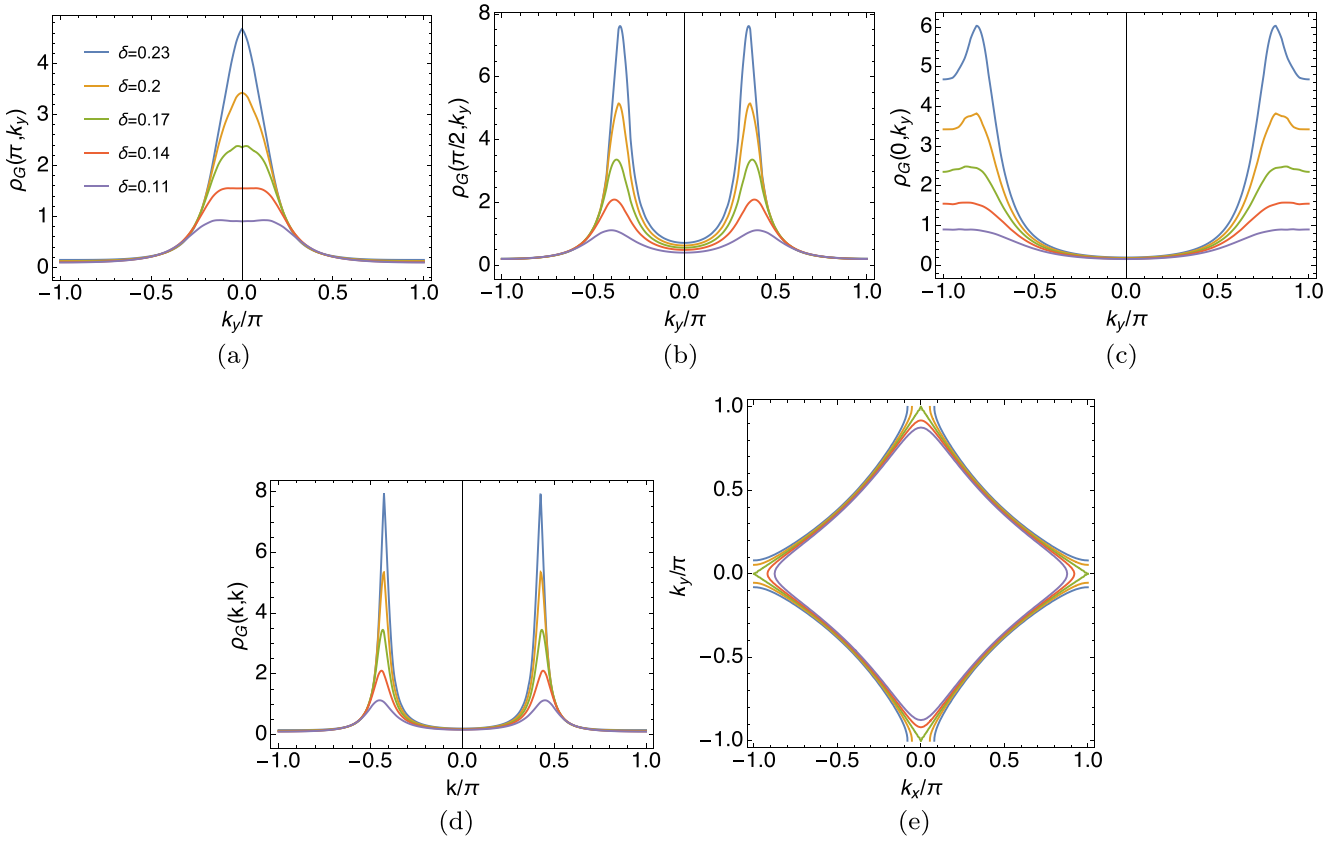

FIG. 8. The spectral function peak height in typical directions of momentum space at several dopings at $t' = -0.2$ and $T = 63$ K. All panels share the same legend. Panel (a) shows evidence of Lifshitz transition (Fermi surface changed from opened to closed) at $\delta \approx 0.17$, similar to the tight-binding model case shown in panel (e). Panels (b), (c), (d) provide other angles to observe this transition, in complementarity with the 3D plots in Fig. 7. (a) $\rho_G(\pi, k_y)$, $M \to X$. (b) $\rho_G(\pi/2, k_y)$. (c) $\rho_G(0, k_y)$, $\Gamma \to M$. (d) $\rho_G(k, k)$, nodal ($\Gamma \to X$). (e) Tight-binding model.

In Fig. 14, from the electron-like panels [(a), (c), (e)] to the strongly hole-like panels [(b), (d), (f)], the LDOS peak shifts from $\omega > 0$ to $\omega < 0$. In contrast to the noninteracting tight-binding model in (e) and (f) where the peak height is independent of doping, (a)–(d) have smaller peaks in general and show that the height decreases at smaller doping with more weight in the lower Hubbard band (insets). This is again a feature of strong correlation. As the system approaches the half-filling limit ($\delta \to 0$), the correlation enhances and further suppresses the quasiparticle peak, which contributes to the central peak of the LDOS. We also observe that (a) is similar to the density dependence of the location of Kondo or Abrikosov-Suhl resonance in the Anderson impurity problem [16]. It can be understood as a generic characteristic in strongly correlated matter given the relation between density and the effective interaction.

B. Resistivity

We next present the resistivity under strong electron-electron interaction. The popular bubble approximation is used and the current correlator is writen as $\langle J(t)J(0)\rangle \sim \sum_k v_k^2 \mathcal{G}^2(k)$. Here the velocity $\hbar v_k^\alpha = \frac{\partial \varepsilon_k}{\partial k_\alpha}$ represents the bare current vertex. In tight-binding theory the sign oscillation in v_k^α leads to a reduction in the average over the Brillouin zone and therefore diminishes the magnitude of the vertex corrections. Also the weak k dependence of self-energy in Fig. 3 reduces the importance of vertex corrections.

In our picture of a quasi-two-dimensional metal, there are 2D well-separated sheets, by a distance c_0 in the c

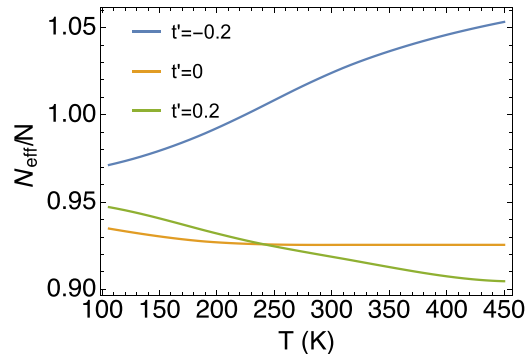

FIG. 9. $N_{\rm eff}/N$ vs T at $\delta = 0.15$ and various t'. For electron-doped ($t' \geqslant 0$) case, $N_{\rm eff}$ increases as one lowers the temperature, while in the hole-doped ($t' = -0.2$) case, $N_{\rm eff}$ decreases upon cooling down. At lower temperature, one expects that $N_{\rm eff}$ equals N.

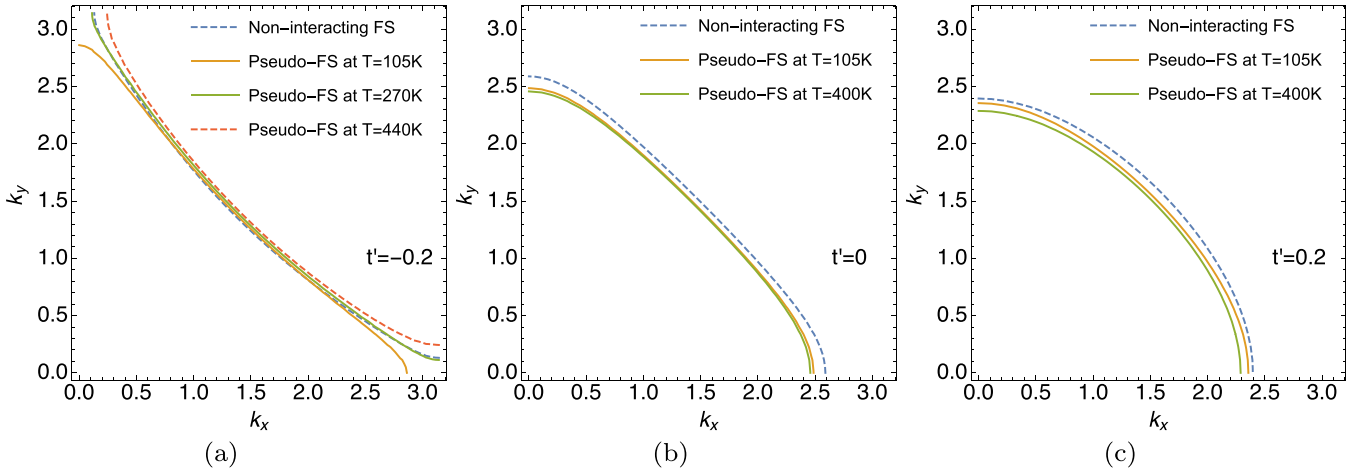

FIG. 10. Comparison between the noninteracting FS and pseudo-FS at low and high temperature. Here we fix $\delta = 0.15$ and vary t'. Generally, as we cool down the system, the pseudo-FS approaches the noninteracting system or FS from the right ($t' = -0.2$) or left ($t' = 0, 0.2$) side. The exception is that at $T = 105$ K and $t' = -0.2$ the pseudo-FS turns out to be closed (electron-like). This delicate effect is a consequence of the redistribution of weight in the spectral function, and its thermal sensitivity is presumably related to the nearby Lifshitz transition point for the choice of $t' = -0.2$. We cannot access very low T for our system sizes, but it is expected that the pseudo-FS flips back to being hole-like at a low T.

direction. Thus each sheet can be effectively characterized by the 2D t-J model. Its dc resistivity ρ_{xx} can be written as follows:

$$\rho_{xx} = \rho_0 \bar{\rho}_{xx} = \frac{\rho_0}{\bar{\sigma}_{xx}}, \tag{12}$$

$$\bar{\sigma}_{xx} = (2\pi)^2 \int_{-\infty}^{\infty} d\omega \left(-\frac{\partial f}{\partial \omega}\right) \left\langle \rho_G^2(\vec{k}, \omega) \frac{\left(\hbar v_k^x\right)^2}{a_0^2} \right\rangle_k, \tag{13}$$

where $\bar{\rho}_{xx}$ and $\bar{\sigma}_{xx}$ represent dimensionless resistivity and conductivity, respectively; $\rho_0 \equiv c_0 h/e^2$ (~ 1.718 mΩ cm)

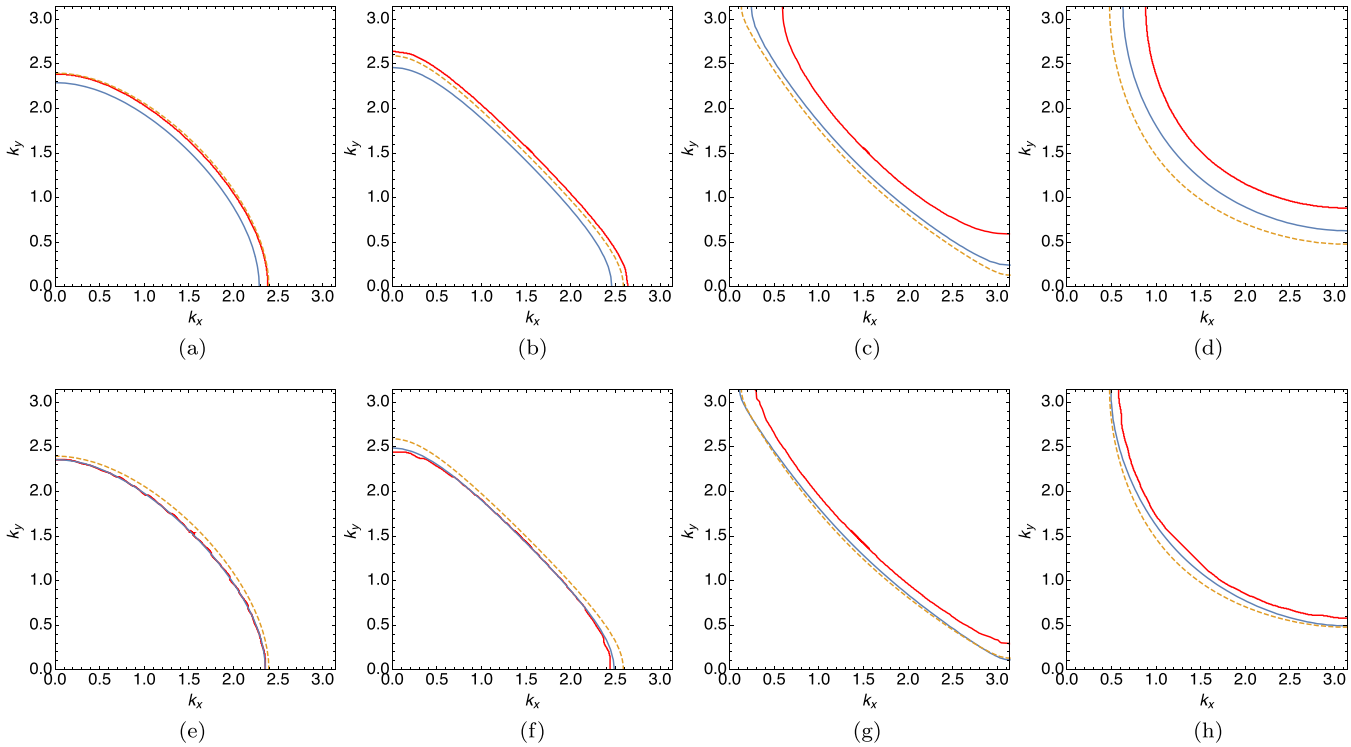

FIG. 11. Comparison between the pseudo-FS from γ_k (blue), the spectral peak (red), and the noninteracting FS (dashed) at various t' and fixed $\delta = 0.15$. Note that the spectral peak (location) curve and the pseudo-FS are not exactly the same, but deviate from the noninteracting FS in the same direction. As T decreases, the difference between them gets smaller. (a) $t' = 0.2$, $T = 400$ K. (b) $t' = 0$, $T = 400$ K. (c) $t' = -0.2$, $T = 440$ K. (d) $t' = -0.4$, $T = 420$ K. (e) $t' = 0.2$, $T = 105$ K. (f) $t' = 0$, $T = 105$ K. (g) $t' = -0.2$, $T = 270$ K. (h) $t' = -0.4$, $T = 105$ K.

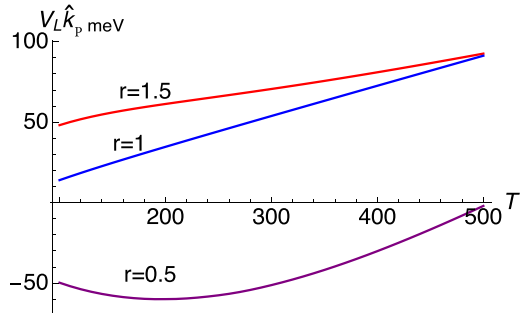

FIG. 12. The location of the peak of the spectral function $A(\hat{k},\omega)$ in Eq. (11) in units of $\hat{k}_P V_L$ versus T, at three values of r. The model spectral function, Eq. (11), is from Ref. [48]. It is obtained by a low-energy expansion of the two ECFL self-energies Ψ and Φ (equivalently χ) in Eq. (2) and Eq. (3). As $T \to 0$ all the curves move towards $\hat{k} = 0$ as one expects, but the approach from finite T displays significant differences depending on the value of r. The values of the parameters used here are $\eta = 0.01$, $\Delta_0 = 50$, $\Omega_\Phi = 5000$ (in meV), and $c_\alpha = 10$. An estimated [48] $V_L \sim 2$ eV Å gives the shift in wave vector $\Delta\hat{k} \sim .05$ Å, at 500 K for $r = 1.5$.

serves as the scale of resistivity; $\langle A\rangle_k \equiv \frac{1}{N_s}\sum_{\vec{k}} A(\vec{k})$; f is the Fermi distribution function. We present our results in absolute units in Fig. 15 by putting the measured values of the lattice constant into the formula and converting the energy unit using $t = 0.45$ eV ≈ 5220 K. The scale of ECFL resistivity is consistent with the experimental findings in cuprates [24].

TABLE I. The Fermi liquid temperature T_{FL} obtained from fitting the data with Eq. (14). Increasing either t' (horizontally) or doping δ (vertically) increases T_{FL}, signaling weaker correlations.

Fermi liquid temperature T_{FL} (K)					
$\downarrow \delta \to t'$	−0.2	−0.1	0	0.1	0.2
0.12	10.0	18.4	33.1	68.2	117.6
0.15	15.8	31.1	66.3	135.4	218.0
0.18	24.4	53.7	117.4	245.2	420.9
0.21	37.3	78.8	189.5	360.3	618.4
0.24	56.8	145.2	274.4	569.5	820.5

In our previous study [15], a significant finding was that the curvature of resistivity changes when t' varies. Here we focus more on the δ-dependent behavior of resistivity as shown in Fig. 15. For a given t', decreasing the hole doping changes the curves from concave to linear then to convex and varying t' shifts the crossover doping region. This phenomenon signals a change of the effective Fermi temperature scale. In higher hole doping (lower electron density), there is less influence of the Gutzwiller projection. Hence the system has less correlation effectively and displays more Fermi-liquid-like behavior, namely, T^2 dependence, and hence positive curvature. In the case with low hole doping, i.e., closer to the Mott-insulating limit, the correlation is relatively stronger and suppresses the Fermi liquid state into a much lower temperature region, which is usually masked

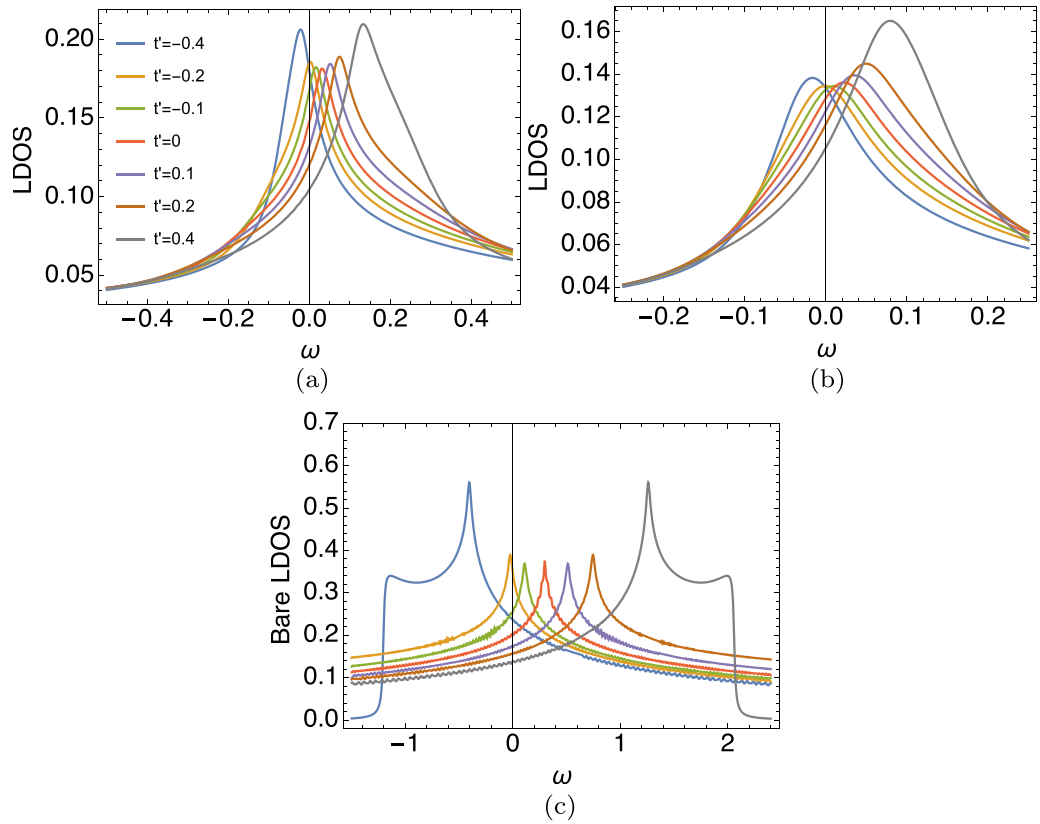

FIG. 13. Local density of states with varying t' while fixing $\delta = 0.15$, at $T = 105$ K and 400 K from ECFL and at $T = 0$ from the bare case. All figures share the same legend. (a) $T = 105$ K. (b) $T = 400$ K. (c) Tight-binding model for reference, $T = 0$.

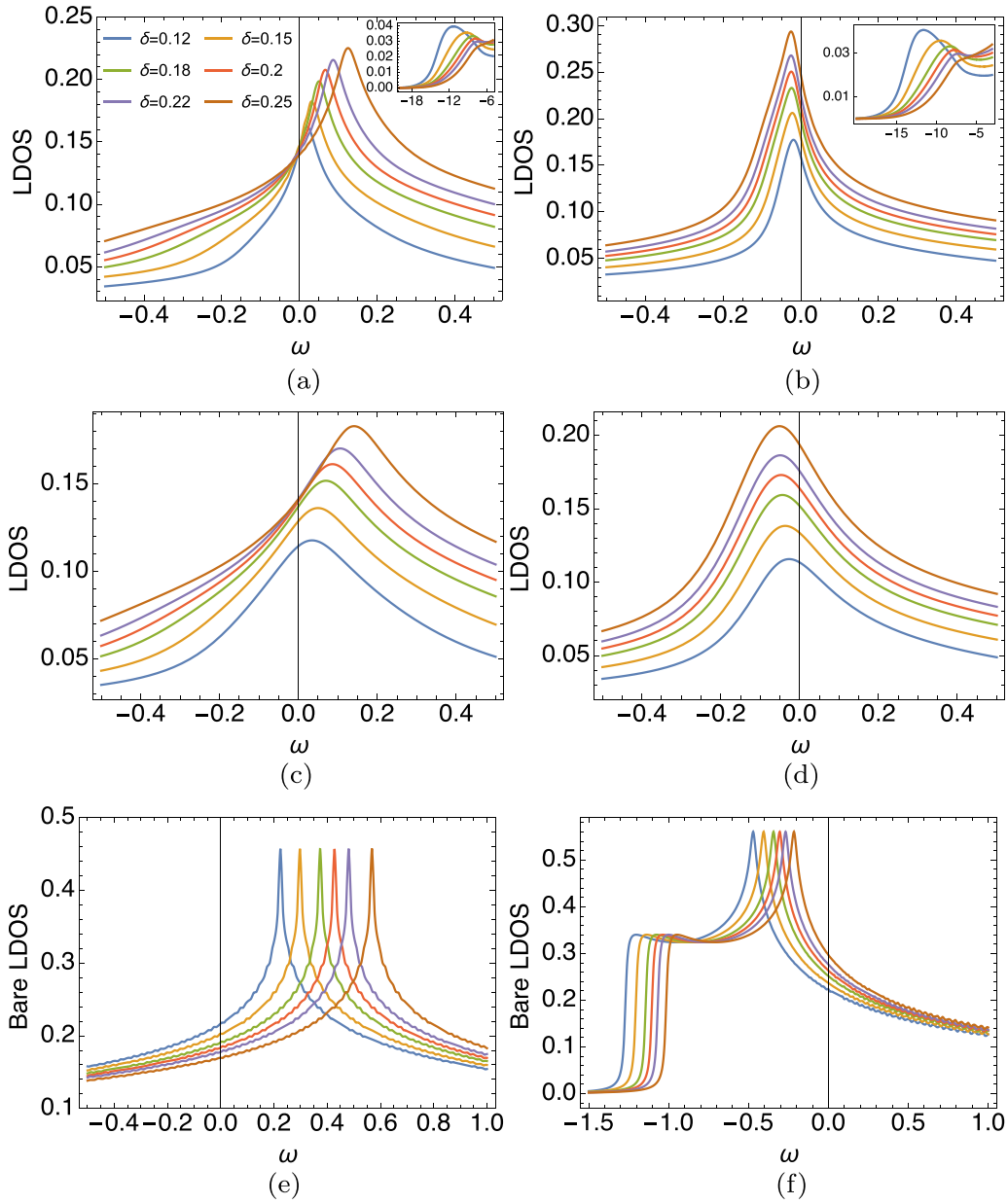

FIG. 14. Local density of states with varying δ while fixing $t' = 0$ and -0.4, at $T = 105$ K and 400 K from ECFL and at $T = 0$ from the bare case. All figures share the same legend. (a) $t' = 0$, $T = 105$ K. (b) $t' = -0.4$, $T = 105$ K. (c) $t' = 0$, $T = 400$ K. (d) $t' = -0.4$, $T = 400$ K. (e) $t' = 0$, tight-binding model for reference, $T = 0$. (f) $t' = -0.4$, tight-binding model for reference, $T = 0$.

by superconductivity. In the displayed temperature range of Fig. 15, the system shows strange-metal or even bad-metal behaviors [17] instead, and hence negative curvature. The curvature can be explicitly calculated as the second derivative of ρ_{xx} with respect to T shown in Fig. 16, which displays features qualitatively similar to the experiments [24,40–43].

To explore the crossover from the Fermi liquid ($\rho_{xx} \propto T^2$) at low T to the strange metal ($\rho_{xx} \propto T$) at higher T, we define a simple fitting model:

$$\rho_{\text{approx}} = \text{const.} \times \frac{T^2}{T_{FL} + T}. \tag{14}$$

This fit gives Fermi liquid behavior for $T \lesssim T_{FL}$ and then crosses over to strange-metal linear behavior at $T \gtrsim T_{FL}$. Thus, T_{FL} serves as a crossover scale describing the boundary of the Fermi liquid region as well as estimating the strength of correlation. We find our data fit into this model well up to intermediate temperature with fitted coefficient and T_{FL}.

Table I shows the value of T_{FL} in various sets of δ and t'. In all cases, the T_{FL} is considerably smaller than the Fermi temperature in the noninteracting case at the order of the bandwidth, as a result of strong correlation. In experiment, a small enough T_{FL} prevents the observation of the Fermi liquid because at low enough temperature the superconducting state shows up instead [24]. Relatively, T_{FL} is further suppressed

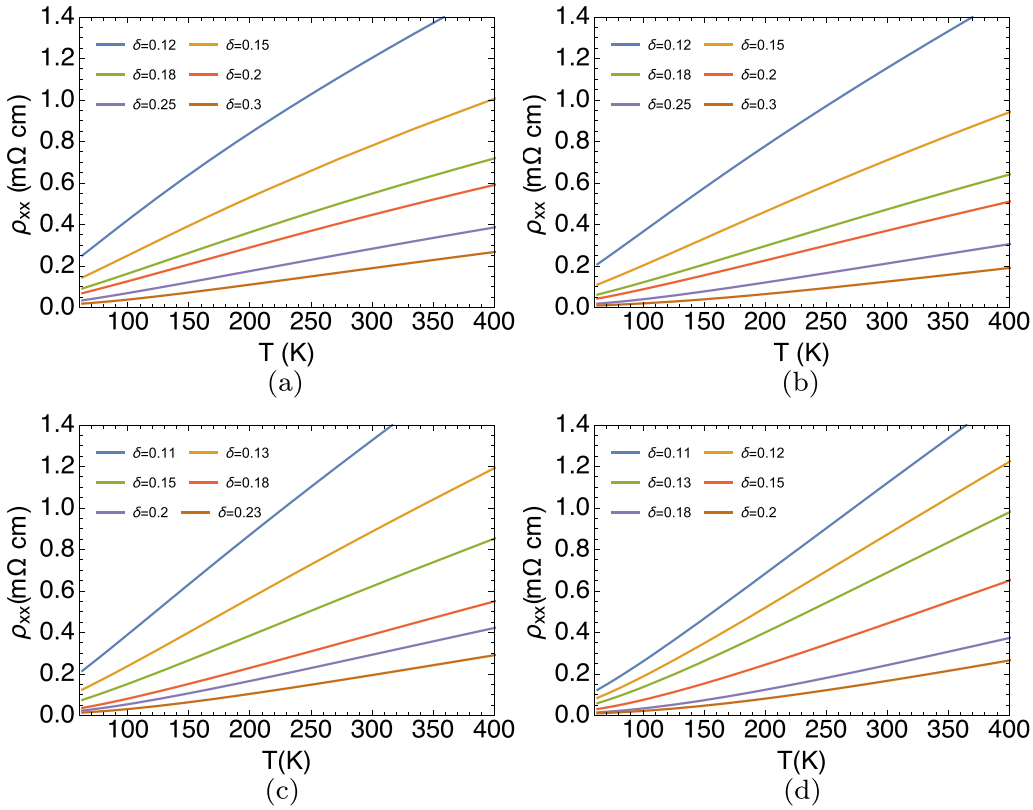

FIG. 15. Resistivity versus T for varying hole doping δ and $t' = -0.2, -0.1, 0, 0.2$ (some data in (a), (b), and (d) can be found in Ref. [15]). The curvature tends to change from negative (convex) to positive (concave) with increasing doping. (a) $t' = -0.2$. (b) $t' = -0.1$. (c) $t' = 0$. (d) $t' = 0.2$.

by smaller second-neighbor hopping t' or smaller doping δ, either of which strengthens the effective correlation. Negative t' increases the resistivity and shrinks the temperature region for the Fermi liquid. In this sense, decreasing t' turns up the effective correlation by depressing the hopping process. On the other hand, decreasing doping leaves less space for electron movement, which also effectively increases the correlation and suppresses T_{FL}. δ and t' both control the effective correlation strength and hence T_{FL}, as shown in Table I. Their similar role can also be understood in the fact that they both change the geometry of the Fermi surface which determines the conductivity at $T \ll W$, where $W = 8t$ is the bare bandwidth. In general, either increasing δ with fixed t' or increasing t' with fixed δ changes the Fermi surface from hole-like to electron-like.

C. Hall number

Within the bubble scheme, we also calculate the Hall conductivity [19,44–46] as $\sigma_{xy} = (-2\pi^2/\rho_0)(\frac{\Phi}{\Phi_0})(\bar{\sigma}_{xy})$. The dimensionless conductivity can be written as

$$\bar{\sigma}_{xy} = \frac{4\pi^2}{3}\int_{-\infty}^{\infty} d\omega\,(-\partial f/\partial\omega)\left\langle \rho_G^3(k,\omega)\eta(k)\right\rangle_k, \qquad (15)$$

where $\eta(k) = \frac{\hbar^2}{a_0^4}\{(v_k^x)^2\frac{\partial^2\varepsilon_k}{\partial k_y^2} - (v_k^x v_k^y)\frac{\partial^2\varepsilon_k}{\partial k_x \partial k_y}\}$; $\Phi = Ba_0^2$ is the flux [47], and $\Phi_0 = hc/(2|e|)$ is the flux quantum. In these terms, we can compute the Hall number as

$$n_H = -\frac{1}{4\pi^2}\frac{\bar{\sigma}_{xx}^2}{\bar{\sigma}_{xy}}. \qquad (16)$$

Note that in this definition, the sign of the Hall number is opposite to that in Ref. [15]. In this definition, n_H shares the same sign with the Hall coefficient R_H, consistent with the experimental convention [24,40–43,49–53]. We present the ECFL Hall number n_H in Fig. 17 together with the noninteracting one n_{H0} for comparison. In all cases of different t', n_H is around 60% of n_{H0} and decreasing t' suppresses the scale of n_H. This indicates the reduction of effective charge carrier due to strong correlation. Therefore, the Hall number increases when the effective correlation turns down either by increasing t' or increasing δ, as shown in Fig. 17. In panel (d), n_H remains smooth when crossing the Lifshitz transition $\delta \approx 0.17$, where the Fermi surface changes from opened to closed as presented in Sec. III A, while n_{H0} shows a crossover to a steeper region.

D. Spin susceptibility and the NMR relaxation rate

The imaginary part of spin susceptibility can also be calculated in the Bubble approximation:

$$\chi''(k,\omega) = \int_{-\infty}^{\infty} dy\langle\rho_G(p,y)\rho_G(p+k,y+\omega)\rangle_p \times [f(y) - f(y+\omega)], \qquad (17)$$

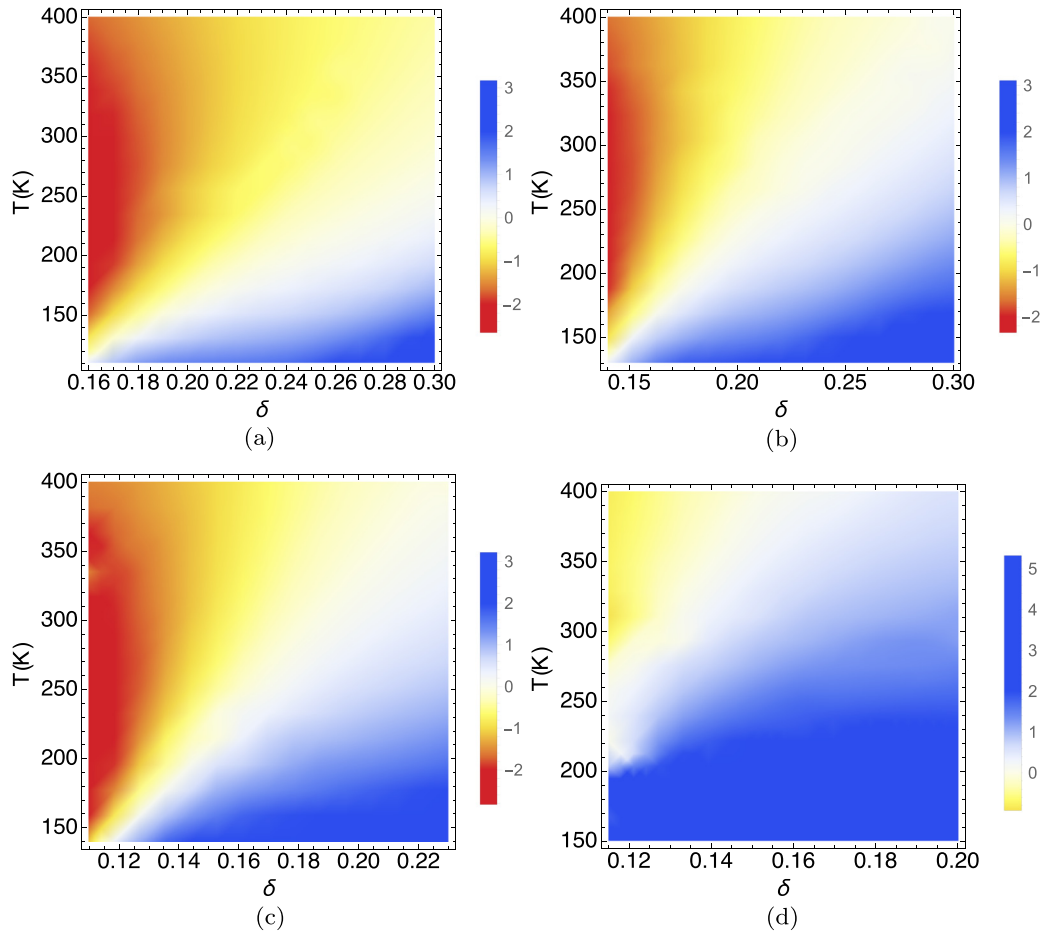

FIG. 16. Curvature of resistivity versus T for a range of doping δ and $t' = -0.2, -0.1, 0$, and 0.2. For most values of t', there is a blue area towards the right bottom representing positive (concave) curvature akin to a Fermi liquid. Towards the left top we find a red area with negative (convex) curvature resembling a strange (or bad) metal [17]. This trend is consistent with experimental results [24]. (a) $t' = -0.2$. (b) $t' = -0.1$. (c) $t' = 0$. (d) $t' = 0.2$.

while the real part χ' can be obtained from calculating the Hilbert transform of χ''. χ'' is shown in Fig. 18 for hole-doped ($t' = -0.2$) and electron-doped ($t' = 0.2$) cases at various fixed k. In both cases, we see the quasielastic peaks in the occupied region for small k which disappears gradually as k increases.

Figure 19 presents the k-dependent χ' at zero frequency, in comparison with the noninteracting χ_0' in the inset. We observe that χ' is much smaller than χ_0' due to the broadening in the spectral function as a result of strong interaction. Despite the scale difference, the k-dependent χ seems closer to χ_0 in the electron-doped case ($t' = 0.2$) than the hold-doped case ($t' = -0.2$), consistent with the previous discussion that the system is more Fermi-liquid-like for positive t'. The Knight shift $\chi'(k = 0, \omega = 0)$ of the system is almost independent of temperature and therefore not shown specifically in figure.

The relaxation rates for cuprates are given by [25,26,55]

$$\frac{1}{T_1} = \frac{\gamma^2 k_B T}{\mu_B^2} \sum_q A_q^2 \frac{\chi''(q, \omega_0)}{\omega_0}, \tag{18}$$

where A_q is a form factor that is determined by the local geometry of the nucleus [25,26,55], and ω_0 is nuclear frequency which is assumed to be very small. Our scheme of calculation is not yet refined enough to capture the detailed difference between the copper and oxygen relaxation rates in cuprates. Hence, we will content ourselves by presenting the case with $A_q = 1$, which should correspond to the inelastic neutron scattering (INS) derived relaxation rate in Ref. [25] from Walstedt *et al.* We plot $1/T_1$ vs T at $\delta = 0.15$ and various t' in Fig. 20. For $t' = -0.2$, $1/T_1$ increases sublinearly with temperature. It shows roughly the same trend as the copper rates shown in Ref. [25], but is somewhat steeper than the derived INS rate therein.

E. J variation

Above we have discussed the ECFL results at $J = 0.17$. We next address the question of variation with J. Figure 21 shows the EDCs and MDCs at different J fixing $t' = 0$. Turning on J raises the peak in EDC [(a) → (c) → (e)] and MDC [(b) → (d) → (f)] slightly. Also, increasing J separates the other EDC lines farther away from $k = k_F$ while bringing the other MDC lines closer to $\omega = 0$.

We find that J has an effect on the effective bandwidth. This can be seen in the EDC and MDC dispersion relation in

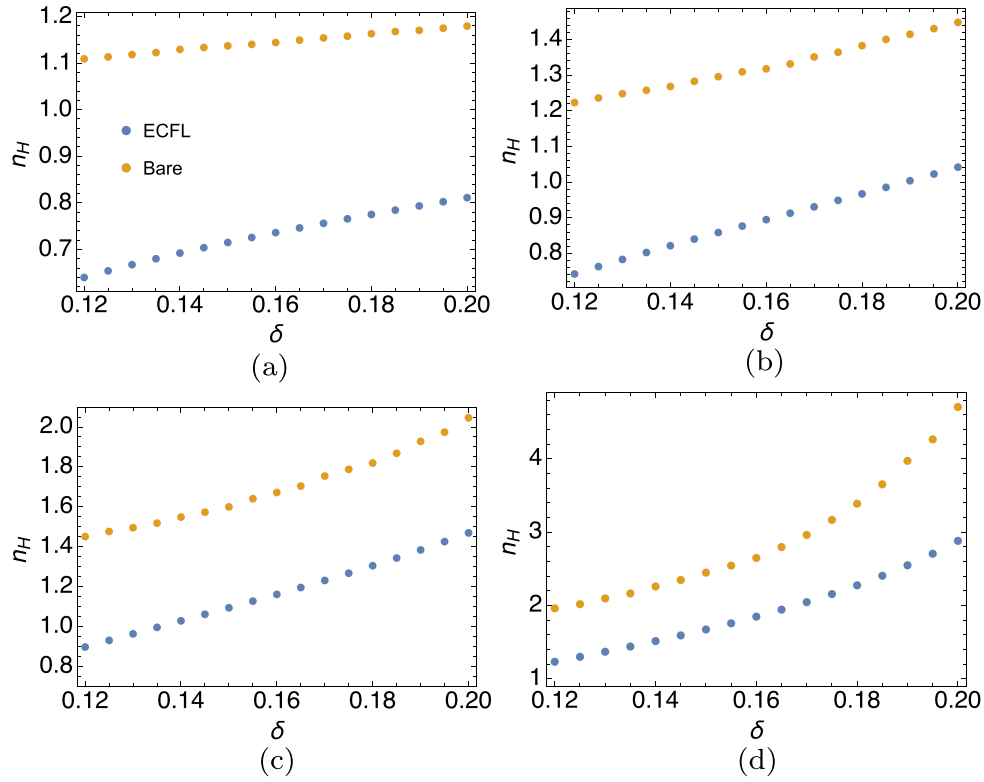

FIG. 17. Hall number vs doping at different t' and $T = 105$ K, where t' controls the scale of n_H. (a) $t' = -0.4$. (b) $t' = -0.3$. (c) $t' = -0.25$. (d) $t' = -0.2$.

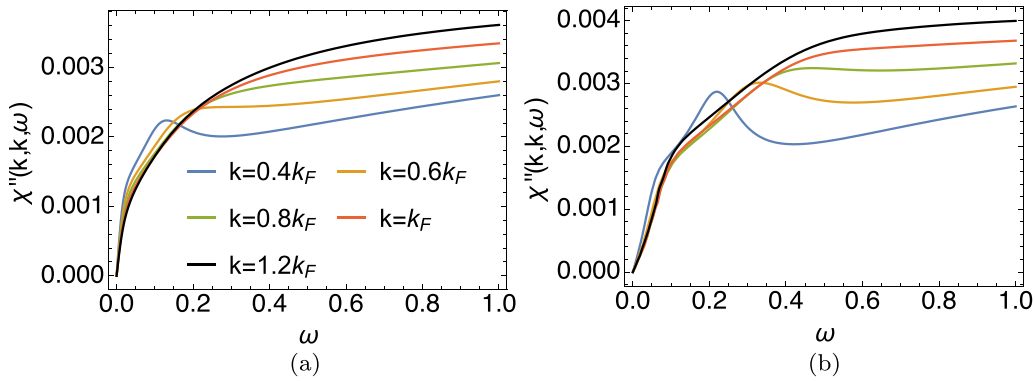

FIG. 18. χ'' at different k for $\delta = 0.15$, $T = 63$ K, and $t' = \pm 0.2$. (a) $t' = -0.2$. (b) $t' = 0.2$.

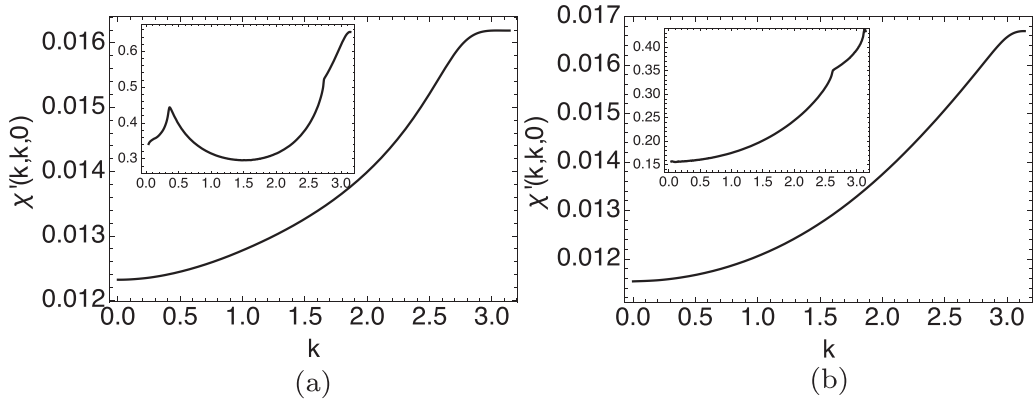

FIG. 19. χ' at $\omega = 0$ for $\delta = 0.15$, $T = 63$ K, and $t' = \pm 0.2$. Inset shows the corresponding noninteracting χ_0'. χ' is largely suppressed from the bare case due to strong interaction. (a) $t' = -0.2$. (b) $t' = 0.2$.

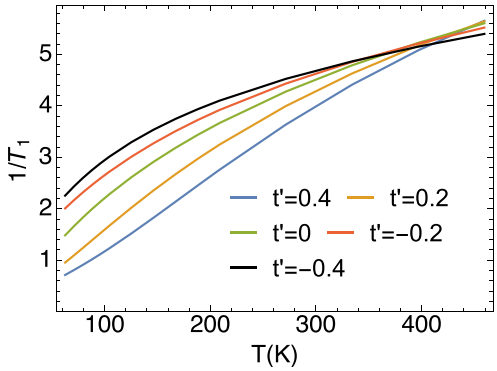

FIG. 20. Relaxation rate from Eq. (18) (arb. units) at $\delta = 0.15$ and different t'. The curve becomes more sublinear as t' decreases from positive to negative. The sublinear curve at $t' = -0.2$ looks similar to the copper relaxation rate in Ref. [25].

Fig. 22. As J increases, the EDC and MDC bands separate out more widely, though they are still very narrow (due to strong correlations) compared to the bare bandwidth. The MDC dispersion shows a high-energy feature, namely the kink (or waterfall). Due to the finite lattice size and to the second-order approximation made in the present work, the low-energy kink discussed in Ref. [48] cannot be resolved clearly. Another angle to view the effect of J is through the 3D plot of the nodal direction spectral function $\rho_G(k, k, \omega)$ in Fig. 23. It appears that turning on J rotates the spectral function counterclockwise with respect to the z axis with $k = k_F$ and $\omega = 0$ if viewed from above. In other words, increasing J extended the renormalized bandwidth with no effect on the Fermi surface location since all curves cross at the same k_F. That said, small variation of J does not change the system behavior qualitatively, and only slightly in

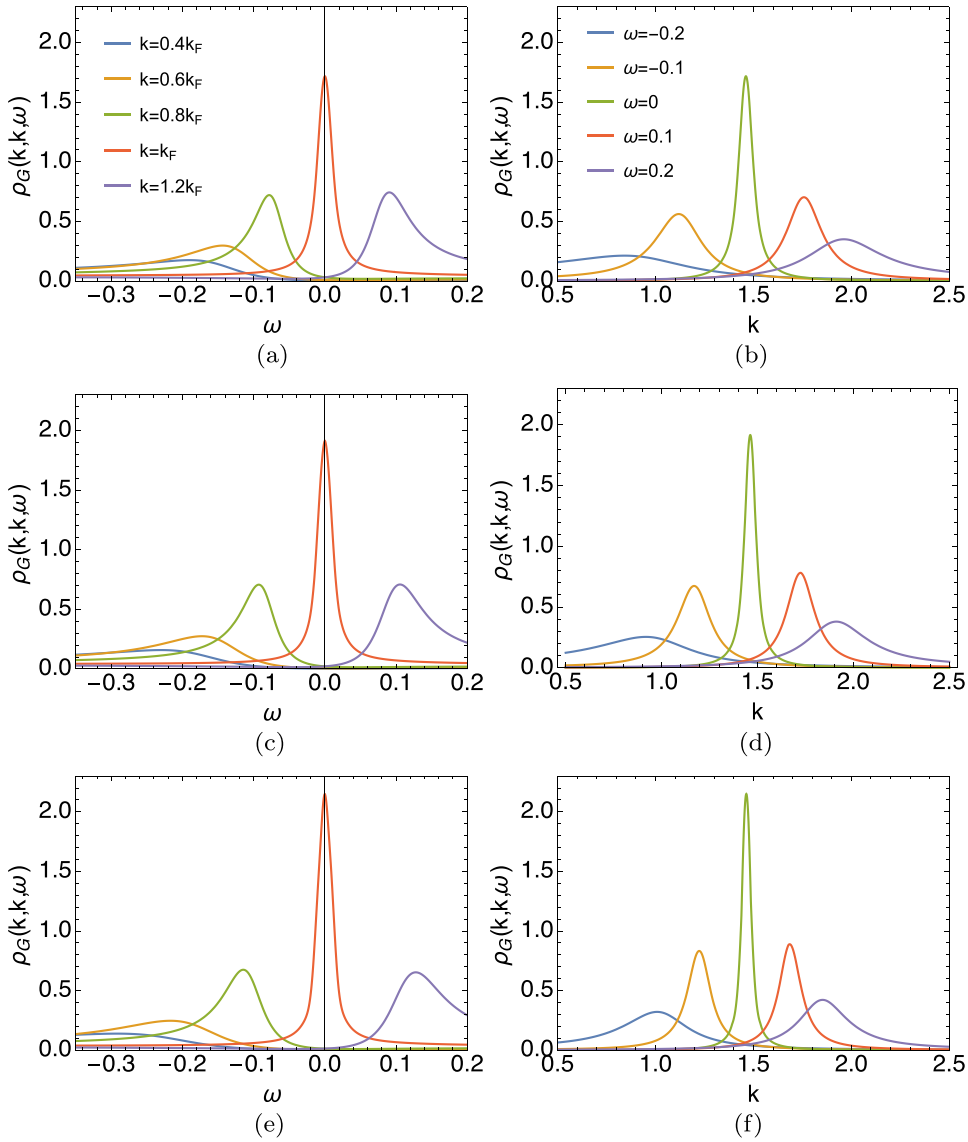

FIG. 21. EDC and MDC line shapes at different values of superexchange J. All EDC figures [(a), (c), (e)] or MDC figures [(b), (d), (f)] share the same respective legend. Here the parameters are set as $\delta = 0.15$, $t' = 0$, $T = 105$ K, and $J = 0, 0.17, 0.4$, in the nodal ($\Gamma \to X$) direction. Increasing J, the peak at the chemical potential becomes somewhat higher, but it remains qualitatively similar at all J. Besides, increasing J separates the EDC lines farther away from $k = k_F$ and brings the MDC lines closer to $\omega = 0$. (a) $J = 0$, EDC. (b) $J = 0$, MDC. (c) $J = 0.17$, EDC. (d) $J = 0.17$, MDC. (e) $J = 0.4$, EDC. (f) $J = 0.4$, MDC.

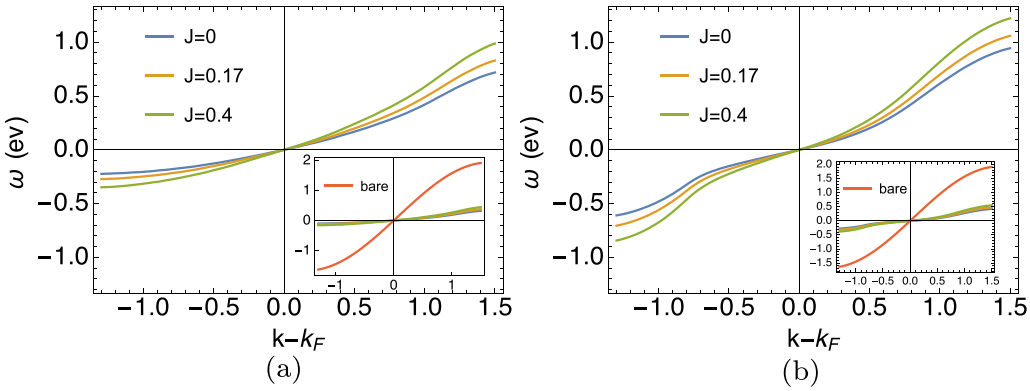

FIG. 22. (a) EDC and (b) MDC dispersion relation at different values of superexchange J. In both cases, increasing J expands the renormalized bandwidth, consistent with Fig. 21 of EDC and MDC lines. Both insets show that the renormalized band is strongly suppressed by correlation compared with the bare one. The energy and k resolution in the present study is not fine enough to deduce the detailed properties of the low-energy kinks (for $\omega \sim 0.07$ eV) discussed phenomenologically within ECFL in Ref. [48].

quantitative detail. Therefore it is reasonable to set $J = 0.17$ from experiment as a representative number and to explore the k, ω, t', and δ dependence of the system.

From the discussion above, we expect the k-average physical quantity like resistivity with significant contribution from the area around the Fermi surface to be insensitive to J variation. Figure 24 shows the resistivity at different J for fixed t'. As expected, varying J from 0 to 0.4 does not make a qualitative difference in the resistivity of the normal state, although it has a relatively stronger effect on the case with larger $|t'|$.

IV. CONCLUSION

We apply the recently developed second-order ECFL scheme [15,16] to studying the 2D t-J model with second-nearest-neighbor hopping t'. We have presented the spectral function, self-energy, LDOS, resistivity, Hall number, and dy-

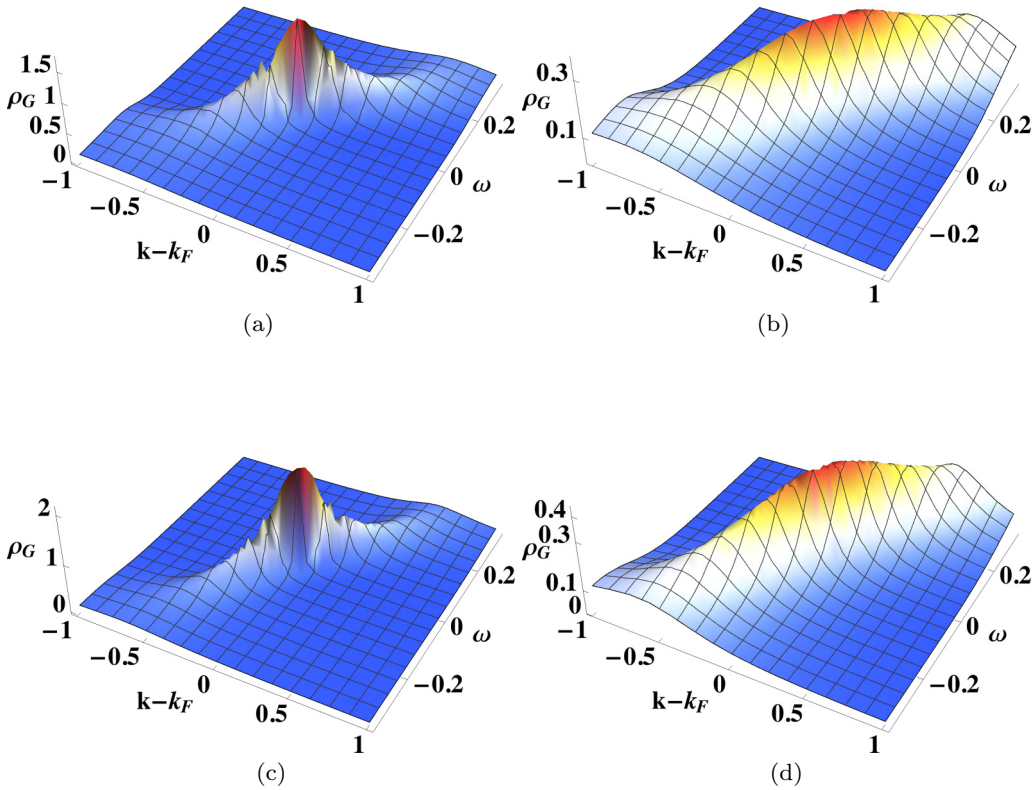

FIG. 23. 3D plot of the nodal direction spectral function $\rho_G(k, k, \omega)$. Consistent with Fig. 21, turning on J increases the peak height and rotates ρ_G counterclockwise with respect to the z axis with $k = k_F$ and $\omega = 0$ if viewed from above. This is another facet of the steeper dispersion with J noted in Fig. 22. (a) $J = 0$, $T = 105$ K. (b) $J = 0$, $T = 400$ K. (c) $J = 0.4$, $T = 105$ K. (d) $J = 0.4$, $T = 400$ K.

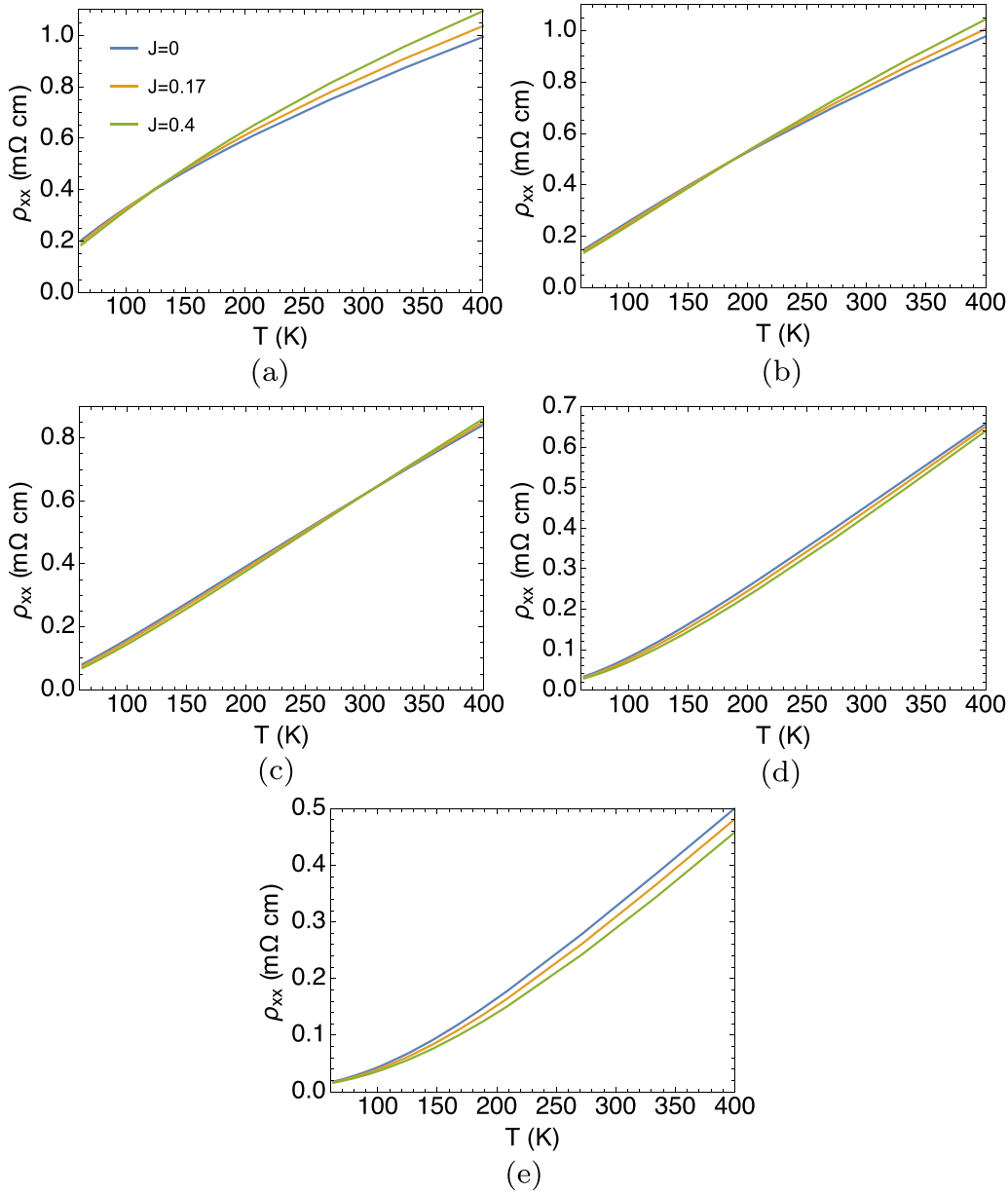

FIG. 24. Resistivity at $\delta = 0.15$ versus T for various J and t' (same legend for all panels). In all t', we observe that J variation of the resistivity is small. As $|t'|$ becomes large J has a somewhat larger influence on the resistivity. (a) $t' = -0.4$. (b) $t' = -0.2$. (c) $t' = 0$. (d) $t' = 0.2$. (e) $t' = 0.4$.

namical susceptibility at low and intermediate temperatures, with t' varying from -0.4 to 0.4 and within a large density region around optimal doping.

The spectral properties are shown to be consistent with ARPES experiments [56–60] on correlated material. The asymmetric EDCs and more symmetric MDCs are observed as expected from the previous study on the phenomenological model of simplified ECFL theory [23]. The weak k dependence of self-energy indicates the relative unimportance of vertex corrections at the densities considered, and gives credence to the use of the bubble approximation for transport.

The curvature change on the resistivity ρ-T curve arises from varying t' and δ, signaling different strength of effective correlation. Both t' and δ affect the effective electron-electron correlation because t' controls the second-neighbor hopping process and δ leaves more or less space for electron movement. As a feature in 2D, the combination of them determines the geometry of the Fermi surface and therefore the low-energy behaviors.

ACKNOWLEDGMENTS

We thank Edward Perepelitsky and Michael Arciniaga for helpful comments on the manuscript. We thank Shawdong Dong for helpful suggestions with the computations. The work at UCSC was supported by the US Department of Energy (DOE), Office of Science, Basic Energy Sciences, un-

der Award No. DE-FG02-06ER46319. Computations reported here used the XSEDE environment [54] (TG-DMR170044) supported by National Science Foundation Grant No. ACI-1053575.

[1] P. W. Anderson, Science **235**, 1196 (1987).

[2] M. Ogata and H. Fukuyama, Rep. Prog. Phys. **71**, 036501 (2008).

[3] G. Kotliar, S. Y. Savrasov, K. Haule, V. S. Oudovenko, O. Parcollet, and C. A. Marianetti, Rev. Mod. Phys. **78**, 865 (2006).

[4] K. Haule and G. Kotliar, Europhys. Lett. **77**, 27007 (2007).

[5] K. Haule and G. Kotliar, Phys. Rev. B **76**, 104509 (2007).

[6] K. Bouadim, N. Paris, F. Hebert, G. G. Batrouni, and R. T. Scalettar, Phys. Rev. B **76**, 085112 (2007).

[7] T. Maier, M. Jarrell, T. Pruschke, and M. H. Hettler, Rev. Mod. Phys. **77**, 1027 (2005).

[8] E. Gull, A. J. Millis, A. I. Lichtenstein, A. N. Rubtsov, M. Troyer, and P. Werner, Rev. Mod. Phys. **83**, 349 (2011).

[9] A. Go and A. J. Millis, Phys. Rev. Lett. **114**, 016402 (2015).

[10] X. Wang, H. T. Dang, and A. J. Millis, Phys. Rev. B **84**, 014530 (2011).

[11] B. S. Shastry, Phys. Rev. Lett. **107**, 056403 (2011).

[12] B. S. Shastry, Ann. Phys. **343**, 164 (2014); **373**, 717(E) (2016).

[13] F. J. Dyson, Phys. Rev. **102**, 1230 (1956); S. V. Maleev, Zh. Eksp. Teor. Fiz. **33**, 1010 (1958) [Sov. Phys. JETP **6**, 776 (1958)].

[14] E. Perepelitsky and B. S. Shastry, Ann. Phys. **357**, 1 (2015).

[15] B. S. Shastry and P. Mai, New J. Phys. **20**, 013027 (2017).

[16] B. S. Shastry and E. Perepelitsky, Phys. Rev. B **94**, 045138 (2016); R. Žitko, D. Hansen, E. Perepelitsky, J. Mravlje, A. Georges, and B. S. Shastry, *ibid.* **88**, 235132 (2013); B. S. Shastry, E. Perepelitsky, and A. C. Hewson, *ibid.* **88**, 205108 (2013).

[17] W. Ding, R. Žitko, P. Mai, E. Perepelitsky, and B. S. Shastry, Phys. Rev. B **96**, 054114 (2017); W. Ding, R. Žitko, and B. S. Shastry, *ibid.* **96**, 115153 (2017).

[18] X. Y. Deng, J. Mravlje, R. Žitko, M. Ferrero, G. Kotliar, and A. Georges, Phys. Rev. Lett. **110**, 086401 (2013).

[19] W. Xu, K. Haule, and G. Kotliar, Phys. Rev. Lett. **111**, 036401 (2013).

[20] A. Georges, G. Kotliar, W. Krauth, and M. Rozenberg, Rev. Mod. Phys. **68**, 13 (1996).

[21] P. Mai, S. R. White, and B. S. Shastry, Phys. Rev. B **98**, 035108 (2018).

[22] P. Mai and B. S. Shastry, Phys. Rev. B **98**, 115101 (2018).

[23] G.-H. Gweon, B. S. Shastry, and G. D. Gu, Phys. Rev. Lett. **107**, 056404 (2011).

[24] Y. Ando, S. Komiya, K. Segawa, S. Ono, and Y. Kurita, Phys. Rev. Lett. **93**, 267001 (2004).

[25] R. E. Walstedt, T. E. Mason, G. Aeppli, S. M. Hayden, and H. A. Mook, Phys. Rev. B **84**, 024530 (2011).

[26] R. E. Walstedt, *The NMR Probe of High-T_c Materials and Correlated Electron Systems*, Springer Tracts in Modern Physics (Springer, New York, 2017).

[27] Observe that in these equations, an arbitrary shift of the band $\varepsilon_k \to \varepsilon_k + c$ can be absorbed into u_0. Thus the *shift invariance* is manifest to second order in λ.

[28] B. S. Shastry, Phys. Rev. B **84**, 165112 (2011); **86**, 079911(E) (2012).

[29] D. Hansen and B. S. Shastry, Phys. Rev. B **87**, 245101 (2013).

[30] K. Matsuyama and G.-H. Gweon, Phys. Rev. Lett. **111**, 246401 (2013).

[31] J. Chang, M. Shi, S. Pailhés, M. Månsson, T. Claesson, O. Tjernberg, A. Bendounan, Y. Sassa, L. Patthey, N. Momono, M. Oda, M. Ido, S. Guerrero, C. Mudry, and J. Mesot, Phys. Rev. B **78**, 205103 (2008); N. Doiron-Leyraud, O. Cyr-Choinière, S. Badoux, A. Ataei, C. Collignon, A. Gourgout, S. Dufour-Beauséjour, F. F. Tafti, F. Laliberté, M.-E. Boulanger, M. Matusiak, D. Graf, M. Kim, J.-S. Zhou, N. Momono, T. Kurosawa, H. Takagi, and L. Taillefer, Nat. Commun. **8**, 2044 (2017).

[32] T. Yoshida, X. J. Zhou, K. Tanaka, W. L. Yang, Z. Hussain, Z.-X. Shen, A. Fujimori, S. Sahrakorpi, M. Lindroos, R. S. Markiewicz, A. Bansil, Seiki Komiya, Yoichi Ando, H. Eisaki, T. Kakeshita, and S. Uchida, Phys. Rev. B **74**, 224510 (2006).

[33] T. Yoshida, X. J. Zhou, M. Nakamura, S. A. Kellar, P. V. Bogdanov, E. D. Lu, A. Lanzara, Z. Hussain, A. Ino, T. Mizokawa, A. Fujimori, H. Eisaki, C. Kim, Z.-X. Shen, T. Kakeshita, and S. Uchida, Phys. Rev. B **63**, 220501(R) (2001).

[34] B. S. Shastry, arXiv:1808.00405.

[35] F. Ming, S. Johnston, D. Mulugeta, T. S. Smith, P. Vilmercati, G. Lee, T. A. Maier, P. C. Snijders, and H. H. Weitering, Phys. Rev. Lett. **119**, 266802 (2017).

[36] Y. J. Yan, M. Q. Ren, H. C. Xu, B. P. Xie, R. Tao, H. Y. Choi, N. Lee, Y. J. Choi, T. Zhang, and D. L. Feng, Phys. Rev. X **5**, 041018 (2015).

[37] P. Choubey, A. Kreisel, T. Berlijn, B. M. Andersen, and P. J. Hirschfeld, Phys. Rev. B **96**, 174523 (2017).

[38] A. Kreisel, P. Choubey, T. Berlijn, W. Ku, B. M. Andersen, and P. J. Hirschfeld, Phys. Rev. Lett. **114**, 217002 (2015).

[39] K. Fujita, A. R. Schmidt, E.-A. Kim, M. J. Lawler, D. H. Lee, J. C. Davis, H. Eisaki, and S.-i. Uchida, J. Phys. Soc. Jpn. **81**, 011005 (2012).

[40] S. Martin, A. T. Fiory, R. M. Fleming, L. F. Schneemeyer, and J. V. Waszczak, Phys. Rev. Lett. **60**, 2194 (1988).

[41] H. Takagi, T. Ido, S. Ishibashi, M. Uota, S. Uchida, and Y. Tokura, Phys. Rev. B **40**, 2254 (1989).

[42] Y. Onose, Y. Taguchi, K. Ishizaka, and Y. Tokura, Phys. Rev. B **69**, 024504 (2004).

[43] Y. Li, W. Tabis, G. Yu, N. Barišić, and M. Greven, Phys. Rev. Lett. **117**, 197001 (2016).

[44] P. Voruganti, A. Golubentsev, and S. John, Phys. Rev. B **45**, 13945 (1992); H. Fukuyama, H. Ebisawa, and Y. Wada, Prog. Theor. Phys. **42**, 494 (1969); H. Kohno and K. Yamada, *ibid.* **80**, 623 (1988).

[45] For this we additionally assume that the magnetic field vertex also assumes its bare value. This assumption requires further validation in 2 dimensions within the t-J model; hence the results for the Hall conductivity are less reliable than the longitudinal conductivity.

[46] L.-F. Arsenault and A. M. S. Tremblay, Phys. Rev. B **88**, 205109 (2013).

[47] The numerics assume a bct unit cell (a, a, c) with $a = 3.79$ Å and $c = 13.29$ Å. In the expression for ρ_0, c_0 corresponds to the interlayer separation $c_0 = c/2$.

[48] K. Matsuyama, E. Perepelitsky, and B. S. Shastry, Phys. Rev. B **95**, 165435 (2017).
[49] H. Y. Hwang, B. Batlogg, H. Takagi, H. L. Kao, J. Kwo, R. J. Cava, J. J. Krajewski, and W. F. Peck Jr., Phys. Rev. Lett. **72**, 2636 (1994).
[50] Y. Ando, Y. Kurita, S. Komiya, S. Ono, and K. Segawa, Phys. Rev. Lett. **92**, 197001 (2004).
[51] F. F. Balakirev, J. B. Betts, A. Migliori, S. Ono, Y. Ando, and G. S. Boebinger, Nature (London) **424**, 912 (2003).
[52] F. F. Balakirev, J. B. Betts, A. Migliori, I. Tsukada, Y. Ando, and G. S. Boebinger, Phys. Rev. Lett. **102**, 017004 (2009).
[53] J. Takeda, T. Nishikawa, and M. Sato, Phys. C (Amsterdam, Neth.) **231**, 293 (1994) (see especially Fig. 4 therein).
[54] J. Town, T. Cockerill, M. Dahan, I. Foster, K. Gaither, A. Grimshaw, V. Hazlewood, S. Lathrop, D. Lifka, G. D. Peterson, R. Roskies, J. R. Scott, N. W-Diehr, Comput. Sci. Eng. **16**, 62 (2014).
[55] B. S. Shastry, Phys. Rev. Lett. **63**, 1288 (1989).
[56] A. Damascelli, Z. Hussain, and Z.-X. Shen, Rev. Mod. Phys. **75**, 473 (2003).
[57] W. S. Lee, I. M. Vishik, D. H. Lu, and Z.-X. Shen, J. Phys.: Condens. Matter **21**, 164217 (2009).
[58] J. D. Koralek, J. F. Douglas, N. C. Plumb, Z. Sun, A. V. Federov, M. M. Murnane, H. C. Kapteyn, S. T. Cundiff, Y. Aiura, K. Oka, H. Eisaki, and D. S. Dessau, Phys. Rev. Lett. **96**, 017005 (2006).
[59] T. Yoshida, X. J. Zhou, D. H. Lu, S. Komiya, Y. Ando, H. Eisaki, T. Kakeshita, S. Uchida, Z. Hussain, Z.-X. Shen, and A. Fujimori, J. Phys.: Condens. Matter **19**, 125209 (2007).
[60] N. P. Armitage, D. H. Lu, C. Kim, A. Damascelli, K. M. Shen, F. Ronning, D. L. Feng, P. Bogdanov, X. J. Zhou, W. L. Yang, Z. Hussain, P. K. Mang, N. Kaneko, M. Greven, Y. Onose, Y. Taguchi, Y. Tokura, and Z.-X. Shen, Phys. Rev. B **68**, 064517 (2003).